07 X 800.   HTC AD 69 12.
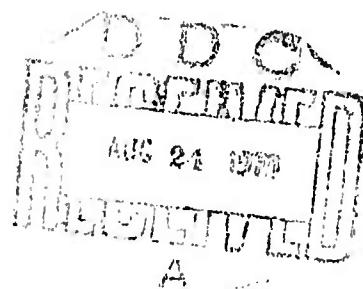
ROTOR/WING
FINAL TECHNICAL REPORT

March 1970

HUGHES TOOL COMPANY · AIRCRAFT DIVISION
Culver City, California
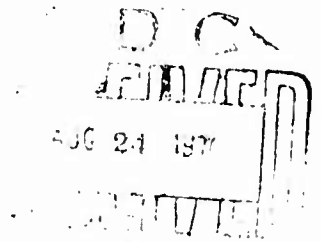
79

397-X-8002   HTC-AD 69-12A

ROTOR/WING
FINAL TECHNICAL REPORT

March 1970

Contract Number: Nonr-4588(00) NR 212-162

HUGHES TOOL COMPANY - AIRCRAFT DIVISION
Culver City, California

FOREWORD

This is the final technical report on an analytical and experimental investigation of the Rotor/Wing concept. The discussion concentrates on the results of the most recent studies and summarizes the current technology -- especially that associated with the transition between the helicopter and the airplane flight modes

TABLE OF CONTENTS

LIST OF ILLUSTRATIONS

LIST OF TABLES

SUMMARY

The Rotor/Wing represents a unique concept for high-speed VTOL aircraft employing the stopped-rotor configuration. This concept, originating at Hughes Tool Company - Aircraft Division in 1962, uses a large-centerbody wing in conjunction with three blades to provide lift in the VTOL flight mode in the conventional helicopter manner. During the airplane mode, the wing and blades are stopped and locked to the fuselage to form a modified delta planform. No blade folding or rotor retracting mechanisms are employed; only lightweight retracting fairings are used to provide a clean configuration for cruise.

Eleven series of wind tunnel tests and two whirlstand tests have been completed during the research program. These tests have investigated the aerodynamic characteristics of blade airfoil section and wing planform shape in hover and airplane flight. The most promising configuration from these preliminary tests, from a performance viewpoint, was selected for investigation of the dynamic behavior of the Rotor/Wing in the several flight modes.

AERODYNAMIC PERFORMANCE

As a result of this research, the basic parameters that affect vehicle performance are well understood. Lift and drag characteristics can be predicted for the airplane flight mode for small changes in Rotor/Wing geometry. The effects of compressibility are included in the prediction techniques. The power required to produce lift in the hover mode has been verified by tests. Again, the effects of changing planform shape can be predicted by logical analysis.

PROPULSION

The prediction technique for rotor power available is based on the successful techniques used during the XV-9A research helicopter program. These analytical techniques have been refined to include both the hot-cycle system, where the gases used to drive the rotor are from a core engine, and the warm-cycle system, where both primary engine and bypass gases are used. The propulsion system losses are readily predictable and efficiencies accurately estimated. The prediction of thrust available in the cruise mode is based on engine manufacturer's estimates and follows the identical methodology found in conventional airplane design.

STABILITY AND CONTROL

The control moments produced by the Rotor/Wing blades during helicopter operation are predictable. The horizontal tail's characteristics, in the downwash field behind the wing, are understood for the wing planform shapes investigated in the wind tunnel. Lateral-directional static stability characteristics are readily predictable using data developed during the test program to size the vertical tail. Stability and control characteristics are sensitive to small changes in planform geometry, and predicted characteristics for a final design configuration must be verified by additional testing.

DYNAMIC LOADS

A 1/7th-scale model was designed to be dynamically similar to the Hughes Composite Research Aircraft. When constructed, the blade-root flexibility did not truly represent what could be achieved in a full-scale vehicle. As a result, the model's resonance characteristics do not duplicate the resonance characteristics predicted for a full-scale aircraft, and resonant amplification of loads occurs at undesirable rotor speeds. An analytical technique was used to account for resonance-amplification of loads measured during wind tunnel tests of the transition flight mode.

The measured blade-root loads, corrected for resonance amplification, are higher than predicted or anticipated. Cyclic flapwise bending is 2.5 times anticipated, blade cyclic torsion is almost 3 times the predicted level, and chordwise bending is 1.4 times the scaled CRA design level. The total transition envelope was not investigated because high loads encountered at advance ratios between 0.25 and 0.57 might have endangered the model.

It is possible that the loads measured during the last tests, Series XI, are inaccurate. Certain harmonic components of the measured loads slope the wrong way when plotted against rotor speed. Agreement between the two dynamic model tests, Series IX and Series XI, is erratic. Yet the last test is very consistent within itself and the Rotor/Wing loads agree well with those measured on the concept model, Series X, at infinite advance ratio where structural dynamics of the models do not enter the situation. Clearly, it is not possible to base design information on what appears to be a low predicted level of endurance loads, yet the measured loads appear to be unrealistically high.

At this stage of concept development, aerodynamic and propulsion performance and stability and control have been adequately defined. The prime concern now, once the cyclic load level has been verified, is to find an operating technique, a schedule of control angles, or a Rotor/Wing structural definition that will minimize blade loads and avoid a large structural weight penalty. Additional dynamic-model tests, parallel with analytical studies, are recommended to achieve this goal.

DESCRIPTION OF THE ROTOR/WING CONCEPT

The Hot Cycle Rotor/Wing is a unique concept for high-speed VTOL aircraft that promises the advantages of the helicopter for low-speed flight combined with the high-speed capability and cruise efficiency of the jet airplane. The Rotor/Wing consists of a large hub and three short, wide-chord blades. It functions as a tip-jet-powered helicopter rotor for vertical and low-speed flight and stops in flight to become a fixed-wing for cruise. The fundamental compromise associated with the Rotor/Wing concept is between the conflicting requirements of fixed-wing and rotary-wing flight modes.

The center of a rotor disc is a region that produces little lift. The inboard 20 percent of a typical blade may produce only 5 percent of total lift, and the drag associated with the hub and blade shanks in this center region is usually a large portion of total parasite drag. The Rotor/Wing concept utilizes this inefficient region of the rotor disc to provide a lifting surface for the stopped-rotor flight mode. The requirements for the stopped-rotor mode are that this center surface be as large as possible, so that conversion to airplane flight can be made at low flight speed. The helicopter mode requires that lift-producing blades sweep as much of the disc as possible. These conflicting requirements are depicted graphically in Figure 1.

The horizontal scale of this figure, blade-root to blade-tip radius ratio, represents the configurative geometry of the Rotor/Wing. The left-hand side represents a typical helicopter configuration, that is, there is only a very small centerbody and the total disc is swept by lift-producing blades. The right-hand side depicts the opposite extreme, the configuration is an equilateral
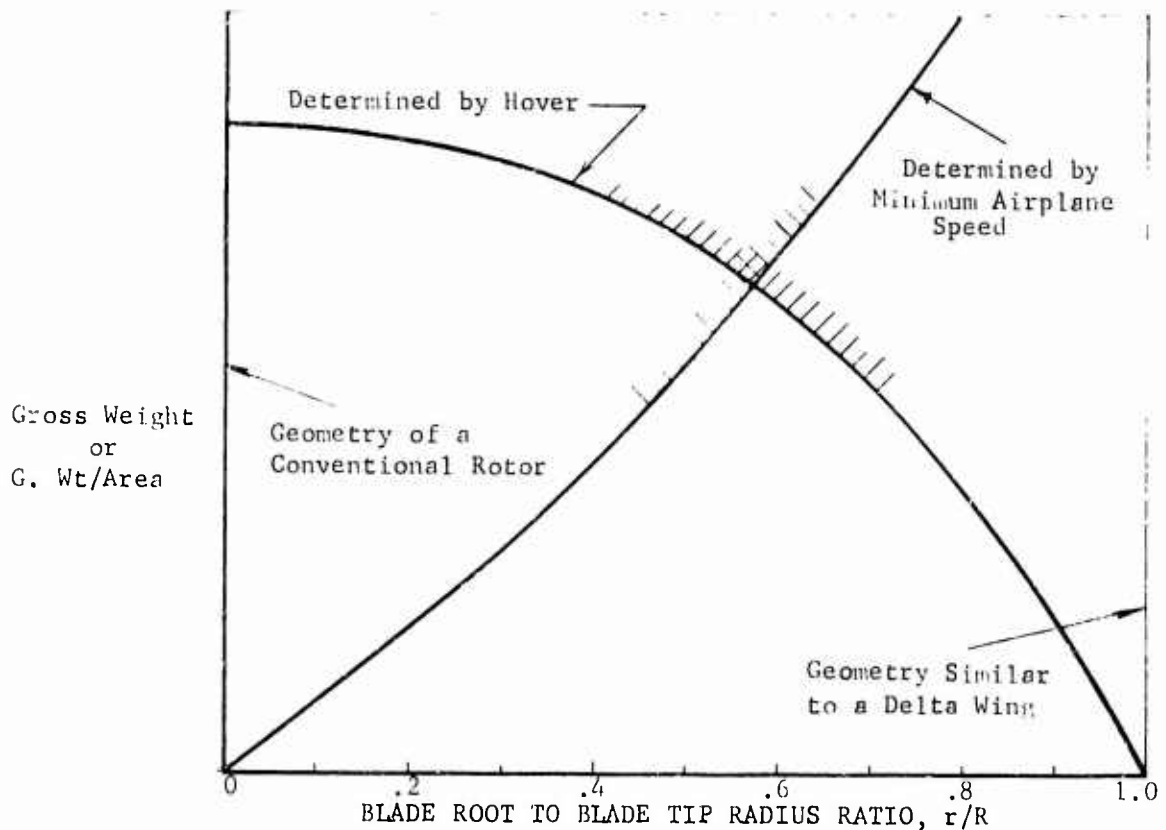
Figure 1. Conflicting Helicopter and Airplane Flight Requirements

triangle inscribed within the circular disc and there are no lift-producing blades. These margins, then, represent the two conflicting requirements, helicopter on the left and airplane on the right.

The Rotor/Wing's lifting ability is depicted on the vertical scale, which may be either gross weight in pounds or disc loading in pounds per square foot of disc area. The diagonal curve, downward to the right, represents the lifting ability in hover flight for constant installed power. The larger the blade span in proportion to the total radius, the larger the weight-lifting capacity during the hover mode. As the center-surface (wing) area increases and blade span decreases, the hover lifting ability decreases -- gradually at first, when the wing utilizes the inefficient disc center, but the curve becomes steeper until, at the right-hand margin, no lift can be produced by the bladeless equilateral-triangle configuration.

The upward sloping curve is determined by the lifting ability of the centerbody surface during the minimum-speed stopped-rotor mode. At the left margin, there is no surface area to produce lift, but, as the surface area increases, the lifting ability in this mode increases rapidly. These two lines represent limits of the conflicting requirements above which the Rotor/Wing concept cannot operate.

The configuration with the largest lifting ability and within the constraints imposed by these requirements lies at the intersection of the two curves. This apex lies between configurations with r/R ratios of 0.5 and 0.6, with lifting ability approximately two-thirds of that attained by a conventional rotor. The exact location of the apex depends upon the power installed, the hover atmospheric conditions, the blade chord, and the speed selected for minimum stopped-rotor flight.

ROTOR/WING OPERATION

Figure 2 shows the operating diagram for the Rotor/Wing concept. The upper left corner represents hover, at a rotor tip-speed of 700 feet per second. The lower right corner represents airplane flight with the Rotor/Wing stopped and locked to the fuselage at 200 knots. The essential feature of the concept is that there is some reasonable path between these two operating points that can be followed in a logical manner. The path shown on Figure 2 was derived to avoid the high blade-tip dynamic pressure that occurs in the upper right corner.

In operation, the Rotor/Wing aircraft takes off, hovers, and flies at speeds up to approximately 100 knots in the helicopter mode, with the rotor powered by its tip jets at constant tip-speed. Aircraft control is from rotor-blade cyclic and collective pitch, plus the yaw fan in the tail. This operation is depicted by the horizontal line at constant 700-foot-per-second tip-speed, ending at an advance ratio of 0.25.
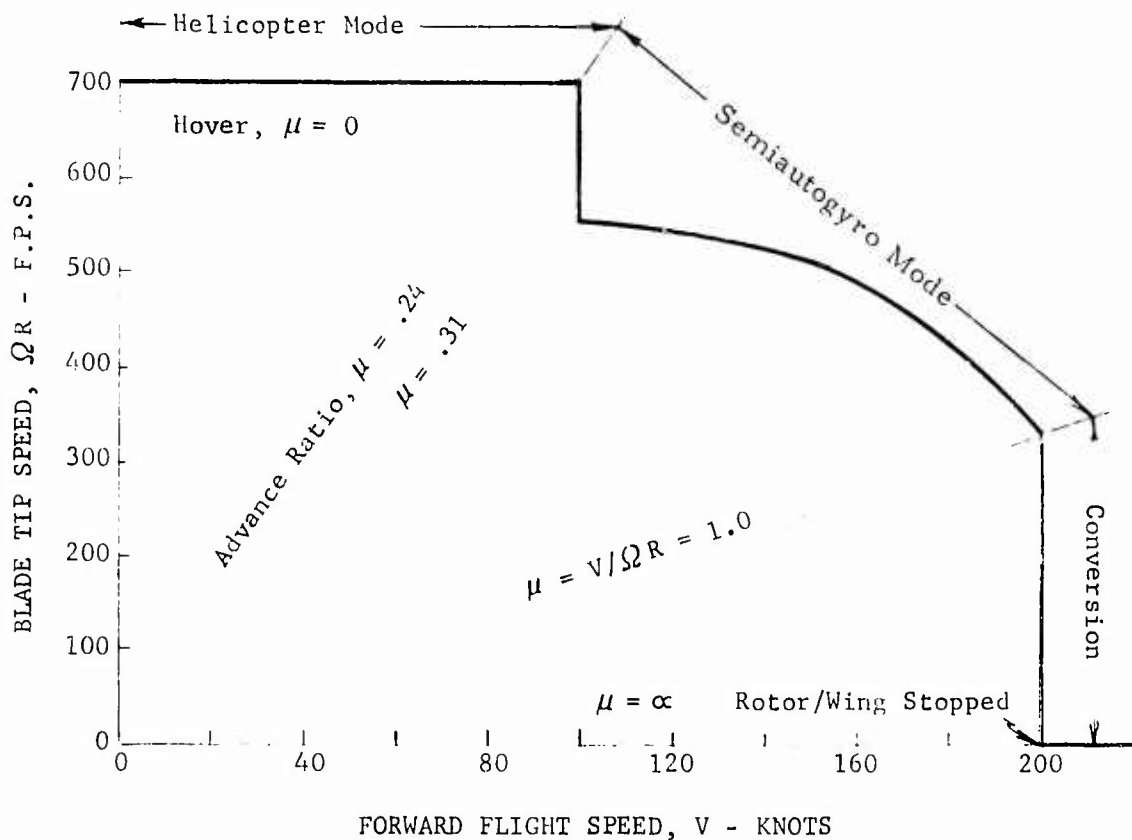
Figure 2. Rotor/Wing Operating Diagram

Flight speed is further increased by shifting power from the rotor to either jet nozzles or to tip turbine cruise fans to produce forward thrust. The exact details and schedule of this operation depend on the configuration; however, the power transfer from one system to the other will be a two-step sequence. The gas flow from one engine (twin-engine configuration) will be diverted to the thrust-producing device, initially. After rotor speed has stabilized at approximately 85-percent of that used as a helicopter and the aircraft has accelerated, the gas from the remaining engine will be diverted from the rotor. This mode, labeled semiautogyro on the figure, is not true autorotation, because power is supplied to drive the rotor directly. Aircraft control is by rotor cyclic pitch augmented by the control surfaces and yaw fan at the tail. The pilot's authority over blade pitch is gradually diminished until, at an advance ratio of 1.00, vehicle control is provided exclusively by the tail surfaces. Rotor deceleration during the sequence from 340 feet per second

7

to zero is provided by both aerodynamic torque and rotor braking. A locking/ indexing mechanism must be provided to position the Rotor/Wing for the air-plane mode.

DESCRIPTION OF THE ROTOR/WING PROGRAM

The purpose of the Rotor/Wing research program has been to develop the analytical techniques that can be used to predict basic loads on vehicle components and predict vehicle performance, stability, and controllability. The program has followed the classic formula for research activities -- develop a theory, conduct tests to verify the theory, and develop an analytical model of the vehicle based on the verified theory. The flow diagram for this technical approach is shown schematically in Figure 3.

Historically, the first questions to be answered about the Rotor/Wing concept concerned hovering performance. Helicopter theory predicted acceptable hover performance, even with a 50-percent centerbody; however, the symmetrical double-ended blades presented some analytical uncertainty. The first research was conducted on the whirlstand at Hughes to answer some of these questions. This test, Whirlstand Series I, was started late in 1962, as shown on the chart of Figure 4. This test compared three centerbody shapes and three double-ended symmetrical airfoils with a conventional helicopter rotor equipped with 0015 blades. These models were pneumatically driven by compressed air expelled from tip nozzles; construction was carved mahogany over a steel frame. Essentially, this test confirmed the helicopter-based hovering theory after suitable adjustments and factors were included for the Rotor/Wing configuration.

With the ability to predict hovering performance confidently established, the next task was to measure the forces and moments on a Rotor/Wing configuration during stopped-rotor forward-flight operation. This would establish the
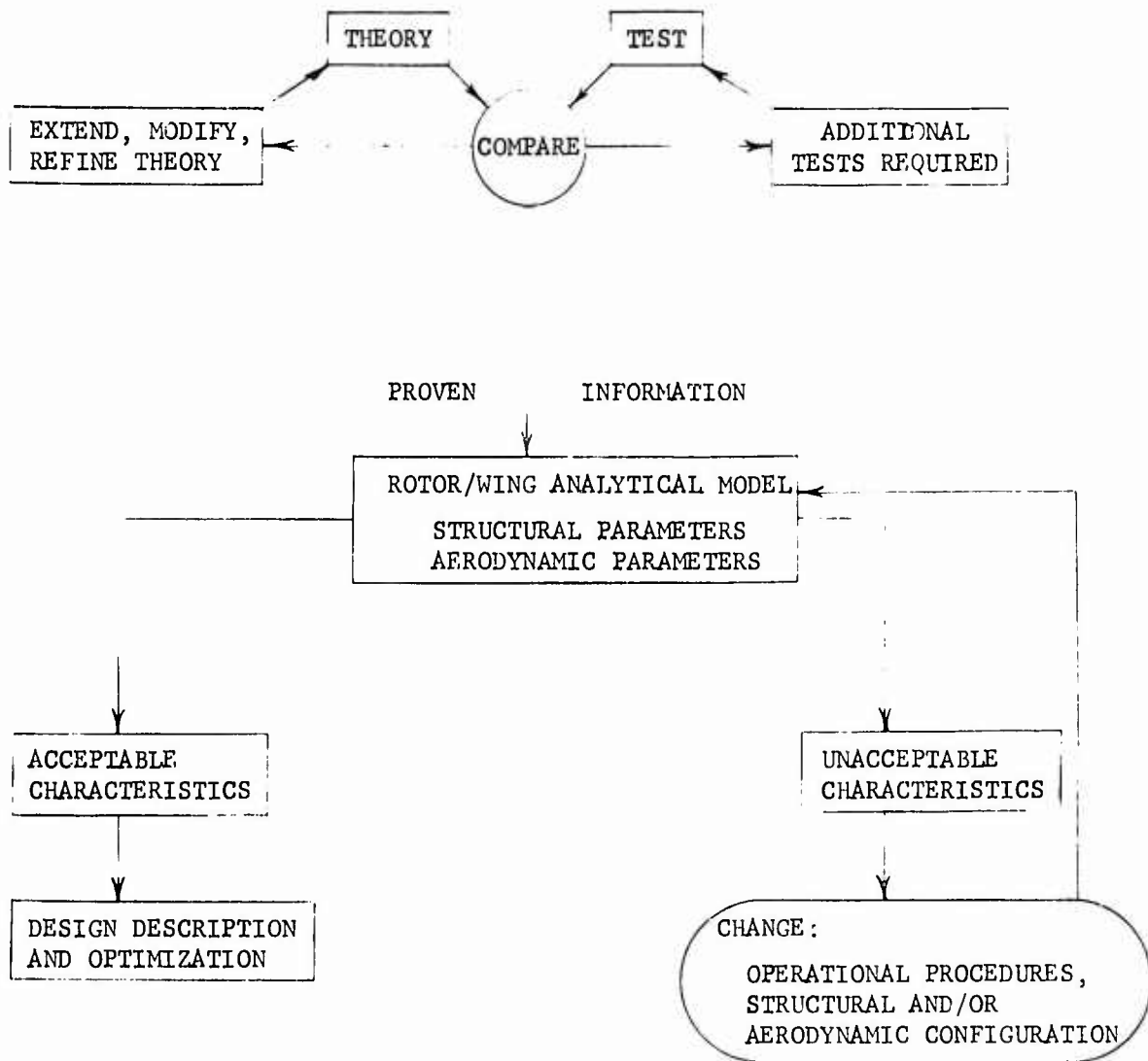
Figure 3. Rotor/Wing Technical Approach
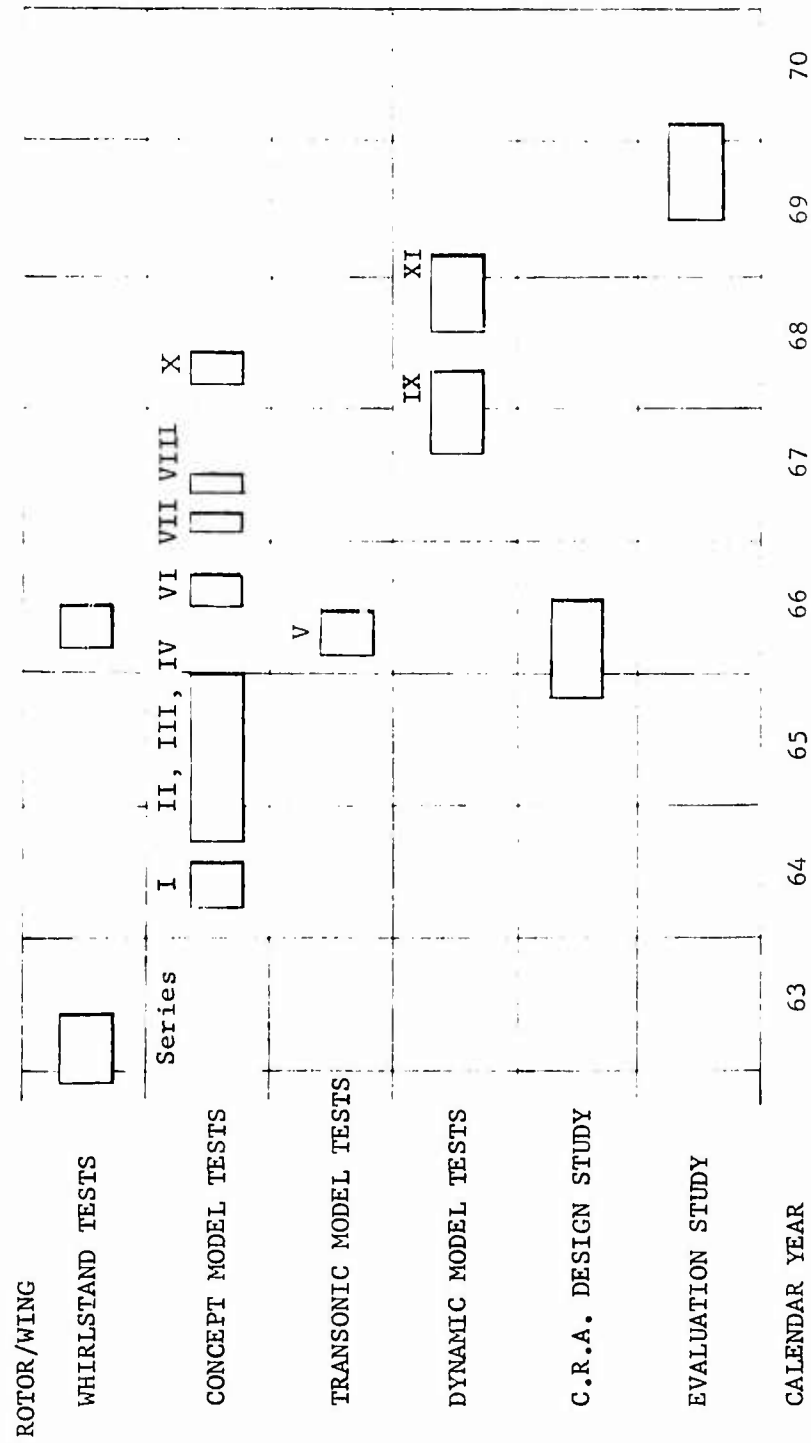
Figure 4. Chronology. Rotor/Wing Research and Development

two corners of the operational envelope shown in Figure 2. The Series I
wind-tunnel test used two of the models developed for the whirlstand. These
models were tested in the low-speed tunnel at the Naval Ship Research and
Development Center, at various rotor azimuth positions, with and without
blades, but without a fuselage. As far as can be determined, these were the
first tests of this kind ever made.

The Series II and Series III tests were conducted to establish data within the
operational envelope, and to demonstrate the stopping and starting of the rotor
by aerodynamic force. This test was moderately successful; only mean forces
and moments could be measured on the tunnel's mechanical balance. Internal
friction within the model's drive system was large compared with aerodynamic
torque; thus, the rotor-turning performance data was subject to the small-
difference-of-large-numbers type of error. The fuselage of this model was
designed to house the model's mechanical components, with little attention
given to fairing and streamlining.

After analysis of this test, it was apparent that the Rotor/Wing configuration
would evolve with tapered blades rather than with the straight, untapered
blades already tested. This was due to several factors: the first was to pro-
vide the space to pass large amounts of gas through the round feathering bear-
ing at the blade root. This makes a large root chord necessary so that a
moderate thickness ratio is achieved. The second factor was structural,
tapered blades and tapered wings are lighter than straight configurations. At
this point, the straight-blade concept was abandoned in favor of the tapered
design currently being considered. It was also realized that the trisector
centerbody planform shape tested previously offered no real aerodynamic
advantage in any flight mode over a triangular shape, and the triangle configu-
ration offered simplified structural design and easier manufacture.

One penalty paid for the Rotor/Wing configuration is the extremely long fuselage that places the cockpit forward of the rotor disc. This long fuselage is used to fair the forward blade during airplane mode flight and it makes the use of ejection seats for the cockpit crew practical. However, the fuselage volume immediately behind the cockpit cannot be used for disposable loads, because of center-of-gravity travel restrictions. Essentially, the cockpit module is on the end of a cantilever beam, and the penalty paid is one of structural weight. Several designs have been considered that feature a short-nose configuration with an unfaired forward blade. Esthetically, these short-nose configurations leave something to be desired, but the possible weight saving of this arrangement could not be ignored. The primary purpose of the Series IV wind-tunnel test was to measure the aerodynamic performance of two short-nose configurations and compare with that obtained on a conventional long-nose model. This test was conducted at the Douglas Company's small tunnel in Long Beach, California, with a model of nominal 1/30th-scale. The small scale of the models, plus the slow tunnel speed, resulted in a low Reynolds number, so that absolute numerical values of drag were questionable. However, on a comparative basis, the long-nose configuration showed considerable favor over the two short-nose arrangements. Additional tests confirmed that differential horizontal tail incidence could be used for roll control so that blade incidence during conversion could be determined by other criteria.

The Series V model was designed for high-speed testing in the transonic tunnel at NSRDC. This test was designed to verify performance estimates at low-speed, plus indicating the Mach number where drag rise could be expected. In addition, the characteristics of a low-mounted horizontal tail were needed to determine longitudinal stability characteristics. There was some concern about the engine inlet's effect on drag during earlier preliminary design studies, so an internal duct through the model was used to simulate internal

13

engine airflow during testing. This comprehensive series included lateral and directional stability tests along with the usual pitch tests at a series of Mach numbers up to M = 0.90.

This test uncovered what was thought to be a lateral/directional stability problem at high angles of attack. Typical of highly swept configurations, static stability was lost as the nose was raised through α = 15 degrees. Time did not permit detailed investigation of this undesirable characteristic until much later in the program, when the Series VII tests were conducted specifically to investigate lateral/directional stability at high angles of attack.

In the mean time, there was some concern over the effects of tunnel wall on the large models tested during Series I, Series II, and Series III. These models were extremely large for the tunnel test section; model rotor diameter was more than 7 feet and test section width was only 10 feet. No corrections had been made to these test data, so the validity of these tests was questionable.

An opportunity to test in the full-scale tunnel at the Langley Research Center was available in 1966. This made it possible to repeat some of the earlier tests so that a comparison of data obtained in the two tunnels could be made. The model installation at Langley required that the strain-gage balance and some of the hydraulic plumbing be installed immediately below the model, where its interference effect on the models could be significant yet could not be measured by the usual strut interference tests. The result was that drag data could not be presented in the final report of those tests. However, the performances of three Rotor/Wing planform configurations were compared. There appeared to be no significant difference between a triangle wing with tapered blades and the previously tested trisector wing with straight blades. The third configuration, called a tricusp, was inferior in the important rotor-turning flight modes.

The seventh series of tests was conducted to investigate the lateral/directional stability problem discovered during the Series V tests and mentioned earlier. Various "fixes" were tried, without great success; the best solution was to raise the vertical tail height. This configuration maintained lateral and directional stability to considerably higher angles of attack than the basic configuration, which became directionally unstable at $\alpha = 10$ degrees.

The Series-VIII tests were designed to investigate the conversion maneuver at advance ratios above 1.0. Using the 1/7th-scale Concept model tested previously, the following technology was established.

- The centerbody wing provides the major portion of vehicle lift during the slowly-turning rotor flight mode; however, the blades cause 70 percent of the 3-per-rev rotor oscillating moments.

- B_1-cyclic pitch can be useful to reduce these moments; however, cyclic pitch was ineffective in producing steady moments on the model. Thus, cyclic pitch is to be used to reduce oscillating loads and not as a vehicle control parameter.

The tenth series of wind-tunnel tests was essentially an extension of the eighth series, in that the high-advance-ratio region of conversion was investigated. Again, collective flaps were used to improve the shaft cyclic stress. These flaps were considerably improved aerodynamically over those tested earlier, and the configuration was practical from a full-scale design standpoint. The center-of-pressure did move rearward toward the rotor center; however, the total shift was not as large as anticipated. Some residual 1-per-rev stress level was measured, regardless of flap configuration or deflection. The result is that flaps were not recommended for further study because the weight penalty of flaps and their mechanism and actuators far exceeds the penalty involved in building a stronger rotating shaft and bearing.

The cyclic pitch matrix run at infinite advance ratio was the first of its kind performed in a systematic manner. B_1-cyclic pitch does reduce the 3-per-rev pitch and roll moments to zero, but not at the same time. A compromise schedule of B_1 and α has been worked out that minimizes both these moments to easily acceptable levels. The penalty paid for minimizing these oscillations is reduced lift. In order to maintain 1-g lift, the angle of attack must be increased, which in turn raises induced drag. Induced drag is further increased as a result of the narrow effective span loading obtained when B_1 unloads the lateral blades.

The Series IX and Series XI Rotor/Wing wind tunnel tests were conducted using the dynamically scaled model in the NSRDC 8-by-10-foot tunnel. The purpose of the Rotor/Wing dynamic model research program is to further validate the technical adequacy of the concept and systematically identify potential problem areas, in a program continuing the investigations begun with the Rotor/Wing concept model.

Any model of the proper geometric scale can produce data on the external aerodynamic characteristics of the Rotor/Wing, but also a paramount interest in studying the applicability of the concept is obtaining a good idea of the structural dynamics of the Rotor/Wing that accompany the aerodynamics. It has been demonstrated that, for conventional helicopters, the equations of motion can be written to a good enough degree of accuracy that they can be solved by an electronic computer to predict the aerodynamics and structural dynamics closely for low advance ratios. This should also be true for the Rotor/Wing, but since it has many operational features that are different from conventional rotors, some assurance of the accuracy of the computational methods was desired. The best way is to compare analytical studies with a dynamically scaled model. The dynamically scaled model is, in itself, an analog computer that automatically writes and solves all the applicable equations of motion for comparison with the solution of equations written for an electronic computer.

16

The model was designed and built for Froude number similarity in air, with consideration given in the design features to accommodate testing in Freon at a later date for Mach number similarity. The model was a 1/7th-scale simulation of the Hughes AVLABS Hot Cycle Rotor/Wing Composite Research Aircraft described in Reference 1.

The Rotor/Wing itself was to be dynamically scaled, as was the pylon and control system, to that estimated for the CRA design. Provision was included for varying the pylon bending stiffness, the torsional stiffness of the blade control system, and the mass balance of the blades. Table 1 shows the comparison of mass and stiffness properties of the wing and blades for the CRA, the Series-IX model, and the Series-XI model at the common CRA scale of R = 25 feet. The Series-IX and the CRA properties compare well; especially so in the blade characteristics.

As a result of the Series-IX tests, it was required to strengthen the blades, which is reflected in the doubled flapwise bending stiffness shown in the table. To compensate for the increased blade stiffness, the redesign incorporated a flapwise flexure at the blade root that would provide a much softer joint more in line with the original CRA design. In operation, the flexure had too much undesirable friction, so Series XI was conducted with a blade much stiffer than desired. In any future test, it will be desirable to lower the stiffness effectively by one-fourth, so that the model frequencies can be cut in half. Because of the model's high stiffness, the collective bending mode was in 3-per-rev resonance at the model's design operating speed - 740 rpm. Thus, the test (Series XI) was conducted at a lower rotor speed to avoid resonance-induced loads.

The model's fuselage and empennage are not dynamically scaled but are very light by usual model standards, so that model inertia in pitch is low, but is still 2 to 3 times what would be expected, proportionately, in a full-scale

1.

Table 1. Rotor/Wing Model Mass and Stiffness Properties Compared With the Full-Scale CRA Design

Common-Scale (R = 25 feet) Comparison

Spanwise Location r/R	Mass M			Flapwise Stiffness 10^{-5} EI		
	CRA	IX	XI	CRA	IX	XI
Wing						
0				270.9	602.7	1596.
0.14	0.413	0.755	0.755	251.7	445.7	821.9
0.28	0.756	1.228	1.228	110.5	222.9	412.9
0.46	0.612	0.858	3.332	4.5	76.7	46.8
Blade						
0.62	0.308	0.197	0.551	22.9	22.6	44.9
0.75	0.141	0.155	0.248	12.8	11.8	23.6
0.88	0.178	0.176	0.174	5.0	5.0	5.9
0.97	0.031	0.304	0.074			
	Feathering Inertia I_0			Torsional Stiffness 10^{-5} GJ		
Wing						
0				88.0	88.1	88.1
0.18	2810.	4252.	4252.	51.6	51.5	51.5
0.46	388.	503.	503.	5.5	2.5	2.6
Blade						
0.62	113.	71.	185.	14.6	14.6	11.3
0.75	40.	44.	65.	6.4	6.5	4.9
0.91	42.	104.	44.			

design. The model was mounted on a gimbal so that there was restrained freedom about the pitch and roll axis and the model could respond to moments in these directions. (This feature has proved to be most effective in demonstrating oscillations about the center of gravity. This amplitude is remarkably reduced by using B1-cyclic blade pitch, as shown in motion pictures taken during the test.)

In total, five distinct wind-tunnel models have been constructed. There are one 1/30th-scale airplane model, two 1/15th-scale airplane models, and two powered 1/7th-scale models. One of the 1/15th-scale models was tested to $M = 0.9$ in a transonic wind tunnel and its data provide the basis for high-speed flight performance analysis.

The 1/7th-scale Concept model was used to investigate nonstructural configuration changes, such as the addition of flaps to the wing centerbody, changes in tail location, and changes in pylon height and nose configuration. This rugged model is powered by hydraulic pressure and has fully actuated controls.

The most sophisticated is the 1/7th-scale dynamic model, which has a dynamically scaled wing and blade structure, a flexible pylon structure of varying stiffness, and powered rotor and control system. This model is fully instrumented to measure blade, pylon, tail, and total aircraft loads in all flight modes. A unique feature is a gimbal mount that allows the model to pitch and roll during various tests of flight mode operation.

Wind-tunnel model scale, the test series, and the reference where the test is reported are summarized on the following page.

Model Scale	Test Series	Reference
1/30th	IV	2
1/15th (Transonic)	V	3
1/15th	VII	4, 5
1/7th (Concept)	I, II, III, VI, VIII, X	6, 7, 8, 9, 10, 11, 12, 19
1/7th (Dynamic)	IX, XI	Unpublished

The two whirlstand tests of the 1/7th-scale Concept model are reported in References 13 and 14.

TECHNICAL DISCUSSION

GENERAL

The sequence of topics presented in this discussion follows the development sequence of the Rotor/Wing concept. As mentioned previously, the first concern was hover performance, followed by performance characteristics in the airplane cruise mode. In the course of performance testing, deficient static stability characteristics were discovered, which were subsequently remedied during the course of further testing. The area of current immediate concern -- dynamic loads on the Rotor/Wing itself -- was the subject of the last series of tests, and is presented as the closing topic of this discussion.

HELICOPTER HOVER MODE ROTOR POWER REQUIRED

The total power required to drive the Rotor/Wing in hover is divided into three parts that can be analyzed separately. These are induced power, profile power, and the power required to drive the centerbody-wing. The analytical methods, as well as the whirlstand substantiation, are presented in this section.

ROTOR-INDUCED TORQUE

The Rotor/Wing configuration has a large centerbody that is equivalent to a large root cutout in a conventional rotor. In order to correctly account for this cutout, the induced torque must be integrated from the blade root radius, AR, to the effective tip radius, BR, instead of the usual value of 0 to BR.

The derivation of the induced-torque equation used in the Rotor/Wing hover analysis is described below; it follows the procedure of Reference 15.

$$T = b \frac{\rho}{2} \Omega^2 \, a \, (\theta_t - \phi_t) C \int_{AR}^{BR} \frac{R}{r} \, r^2 \, dr$$

Integrating this equation:

$$T = b \frac{1}{2} \rho \, \Omega^2 \, R^3 \, a \, (\theta_t - \phi_t) C \left(\frac{B^2 - A^2}{2} \right) = C_T \pi R^2 \rho \, (\Omega R)^2$$

where:

$A =$ (blade root radius/tip radius) ratio

$B =$ the tip loss factor

Let

$$\sigma = \frac{bc}{\pi R}$$

then

$$\frac{C_T}{(B^2 - A^2)} = \frac{\sigma a}{4} \, (\theta_t - \phi_t)$$

or

$$(\theta_t - \phi_t) = \frac{4C_T}{\sigma a \, (B^2 - A^2)}$$

and

$$\theta_t = \phi_t + \frac{4C_T}{\sigma a \, (B^2 - A^2)}$$

$$\Phi_x = \frac{\sigma a}{16x} \left(-1 + \sqrt{1 + \frac{32 \times \theta_x}{\sigma a}} \right)$$

$\Phi_t = x \Phi_x$ and $\theta_t = x \theta_x$, assuming ideal twist

then

$$\Phi_t = \frac{\sigma a}{16} \left(-1 + \sqrt{1 + \frac{32 \, \theta_t}{\sigma a}} \right)$$

Substitute for θ_t in terms of C_T

$$\Phi_t = \frac{\sigma a}{16} + \frac{\sigma a}{16} \sqrt{1 + \frac{(32)(4) C_T}{\sigma^2 a^2 (B^2 - A^2)} + \frac{32 \, \Phi_t}{\sigma a}}$$

$$\Phi_t + \frac{\sigma a}{16} = \sqrt{\frac{\sigma^2 a^2}{16^2} + \frac{(32)(4) C_T \, \sigma^2 a^2}{(16)^2 \, \sigma^2 a^2 (B^2 - A^2)} + \frac{\sigma^2 a^2 (32) \, \Phi_t}{\sigma a (16)^2}}$$

Squaring both sides and cancelling terms

$$\Phi_t^2 + \frac{2 \sigma a \, \Phi_t}{16} + \frac{\sigma^2 a^2}{(16)^2} = \frac{\sigma^2 a^2}{(16)^2} + \frac{C_T}{2 (B^2 - A^2)} + \frac{\sigma a \, \Phi_t}{8}$$

$$\Phi_t = \sqrt{\frac{C_T}{2 (B^2 - A^2)}}$$

$$Q_i = \int_A^B b \frac{1}{2} \rho \, a^2 R^4 \, a \times (\theta_t - \Phi_t) \, \Phi_t \, c \, dx$$

$$Q_i = b \frac{1}{2} \rho \Omega^2 R^4 a (B^2 - A^2)(\theta_t - \phi_t) \phi_t \, cdx = C_{Q_i} \pi R^2 \rho (\Omega R)^2 R$$

$$C_{Q_i} = \frac{(B^2 - A^2)}{4} \sigma a (\theta_t - \phi_t) \phi_t$$

Substituting for $(\theta_t - \phi_t)$ and ϕ_t above

$$C_{Q_i} = \frac{(B^2 - A^2)}{4} \sigma a \left(\frac{4 C_T}{a (B^2 - A^2)} \right) \sqrt{\frac{C_T}{2 (B^2 - A^2)}}$$

Canceling terms

$$C_{Q_i} = \frac{C_T^{\frac{3}{2}}}{\sqrt{2} \sqrt{B^2 - A^2}}$$

This value of induced torque is derived assuming ideal twist or taper. The table on page 96 of Reference 15 presents a correction factor to be used to correct the induced torque for combinations of taper and the lack of twist. Typical Rotor/Wing blades have a 2.3:1 taper ratio, thus a factor C_1 of 1.04 is added to the induced power, resulting in:

$$C_{Q_i} = \frac{C_i C_T^{\frac{3}{2}}}{\sqrt{2} \sqrt{B^2 - A^2}} = \frac{C_i C_T^{\frac{3}{2}}}{B \sqrt{2} \sqrt{1 - \frac{A^2}{B^2}}}$$

or, in another form:

$$\frac{C_{Q_i}}{C_i C_T^{3/2}} = \frac{1}{B \sqrt{2} \sqrt{1 - \frac{A^2}{B^2}}}$$

PROFILE POWER

The profile torque coefficient is computed using the basic equation (36) on page 83, Reference 15, written in a slightly different form:

$$\frac{C_{Q_0}}{\sigma} = \frac{\delta_0}{8} + \left(\frac{\delta_1}{3a}\right)\left(\frac{C_T}{\sigma B^2}\right) + \left(\frac{4\delta_2}{a^2}\right)\left(\frac{C_T}{\sigma B^2}\right)^2$$

The values of δ are given by the NACA polar, which is based on conventional airfoils such as an NACA 0012 airfoil.

$$C_{d_0} = 0.0087 - 0.0216\alpha_r + 0.4\alpha_r^2$$

which results in

$$C_{Q_0}/\sigma = \left[0.0010875 - 0.002513\left(C_T/\sigma B^2\right) + 0.0487316 \left(C_T/\sigma B^2\right)^2\right]$$

The solidity used in the above equation is based on a weighted effective chord from A to 100-percent radius; the tip loss factor B of 0.97 handles the tip loss.

The weighted effective chord is given by

$$c_e = \frac{\int_A^1 cx^2\ dx}{\int_0^1 x^2 dx}$$

where:

$$x = \frac{r}{R}$$

$$\sigma = \frac{bc_e}{\pi R}$$

As in the induced power, the factor for planform and twist c_i is applied.

The drag polar used in the profile torque equation is based on 12-percent-thick airfoils; therefore, a factor is added to account for the increased drag of a thicker airfoil. The average thickness is assumed to be the thickness at the radius at which the geometric chord is equal to the effective weighted chord. This value is then 14.4 percent. Airfoil data of Reference 16 indicate an approximate 2.3-percent increase in drag coefficient with each 1-percent increase in airfoil thickness. Therefore, the profile torque is increased by 6 percent to provide an allowance for increased drag over that of the conventional NACA airfoil.

NACA whirl tower tests presented in Reference 17 for a rotor with an NACA 0015 airfoil are used to determine a profile power correction due to stall and compressibility, if required. These data are modified in the following manner for the Rotor/Wing configuration.

It is conservatively assumed that the drag rise due to stall for the circular arc airfoil will occur approximately 1 degree in angle of attack earlier than for an NACA 0015 airfoil. To account for this, the average C_L is increased by an equivalent of 1 degree when entering the profile power-Mach number charts of Reference 17.

The rotor of Reference 17 had -5.5 degrees of twist, whereas the CRA Rotor/Wing is untwisted. Reference 18, which presents whirl-tower test data for both a twisted and an untwisted model rotor, shows that at a constant Mach number the angle for drag divergence is increased by 1 degree for an untwisted blade compared with one with -8 degrees of twist. Thus, the tip angle of attack of an untwisted blade is effectively 1 degree higher, rather than the expected 2 degrees higher, for a blade with -8 degree twist. To apply the drag-divergence data of Reference 17 to the Rotor/Wing configuration in hover, the average lift coefficient is conservatively increased by an equivalent of 2-degree angle of attack (1 degree for lack of twist, 1 degree t

account for the circular arc airfoil), assuming the blade lift curve slope is 0.1 per degree.

The drag divergence data of Reference 17 has been replotted in terms of C_T/σ. The value of the factor determined from this data is identified as C_{stall}.

The resulting equation for profile torque used for Rotor/Wing performance is

$$C_{Q_0} = C_{stall} (1.06) C_i \left[0.0010875 - 0.0025131 \left(C_{T/\sigma B^2} \right) + 0.0487316 \left(C_{T/\sigma B^2} \right)^2 \right]$$

WING HOVER TORQUE

The wing torque is obtained from whirlstand tests of the triangle and trisector wing with blades off. The torque on a rotating flat plate is proportional to the radius taken to the fifth power.

$$C_{Q_W} = C_f \times Area \times V_T^3$$

$$Area \approx R^2$$

and

$$V_T^3 \approx R^3$$

thus:

$$C_{Q_W} \approx R^5$$

A function, Figure 5, which passes through the two data points at the test radius ratio, gives the C_{Q_W} for that wing configuration at all radius ratios.
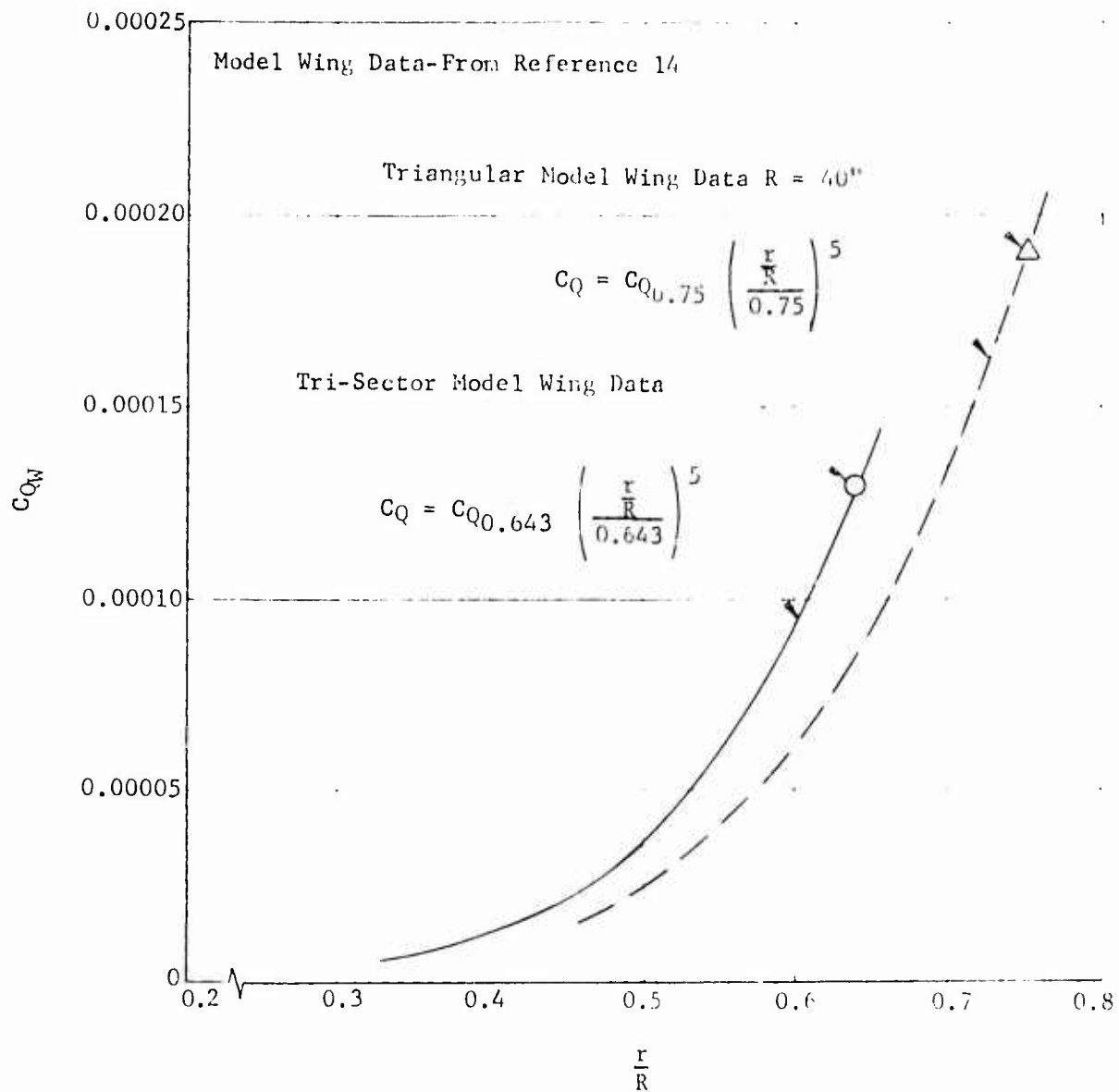
The figure shows a graph with the following labels:

Y-axis: C_{Q_N} with values 0, 0.00005, 0.00010, 0.00015, 0.00020, 0.00025

X-axis: $\frac{r}{R}$ with values 0.2, 0.3, 0.4, 0.5, 0.6, 0.7, 0.8

Model Wing Data-From Reference 14

Triangular Model Wing Data R = 40"

$$C_Q = C_{Q_{0.75}} \left(\frac{\frac{r}{R}}{0.75} \right)^5$$

Tri-Sector Model Wing Data

$$C_Q = C_{Q_{0.643}} \left(\frac{\frac{r}{R}}{0.643} \right)^5$$

Figure 5. Blades-Off Variation of Torque Required in Hover

WHIRL-TOWER MODEL SUBSTANTIATION OF HOVERING PERFORMANCE COMPUTATIONAL METHOD

Data from whirl-tower tests of models of a conventional helicopter rotor with NACA 0015 blades, called herein the reference rotor, and a Rotor Wing with circular arc blades are used to substantiate the power-computing method.

A C_T-C_Q curve from tests of the reference rotor is shown in Figure 6. A profile power factor (PPF) for the model is determined by comparing these test data with a similar curve calculated by the NACA performance method (Reference 15). The PPF thus determined is shown in Figure 7, and is the result of the low Reynolds number of the small-scale model, since both the model and the theory have NACA 0015 blades.

When the profile power factor determined in this way is applied to the hovering computational method devised for the Rotor/Wing configuration with an NACA 0015 airfoil, the good agreement between model test data and C_T-C_Q predicted for the Rotor/Wing model is shown in Figure 9.

The profile power factor for the model tests was computed using the method outlined in this report and is presented in Figure 8. The PPF is consistent between Series I and Series II whirlstand tests. At C_T/σ_T ~ 0.08, the variation of PPF, maximum to minimum, represents ±5 percent of the total C_Q. This is within the scatter of the data.

The figure of merit, M, for the model test, and corrected to full scale, is presented in Figure 10. Figure 3 in Reference 20 presents a figure of merit for a model test and full-scale tests. The figure of merit of Reference 20 shows a correction to full scale similar to that deduced for the Rotor/Wing shown in Figure 10.
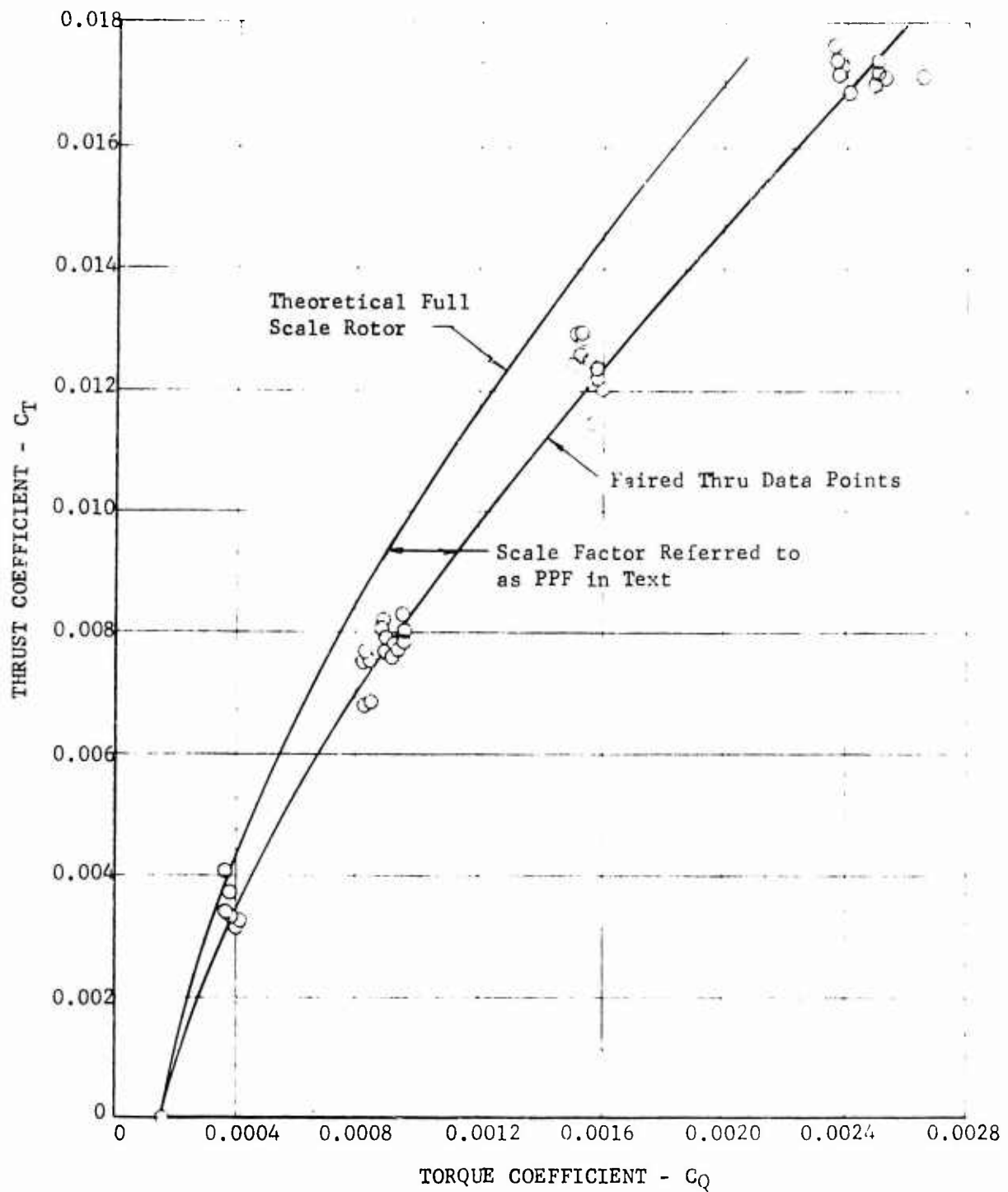
Figure 6. Thrust and Torque Coefficients, Reference Rotor
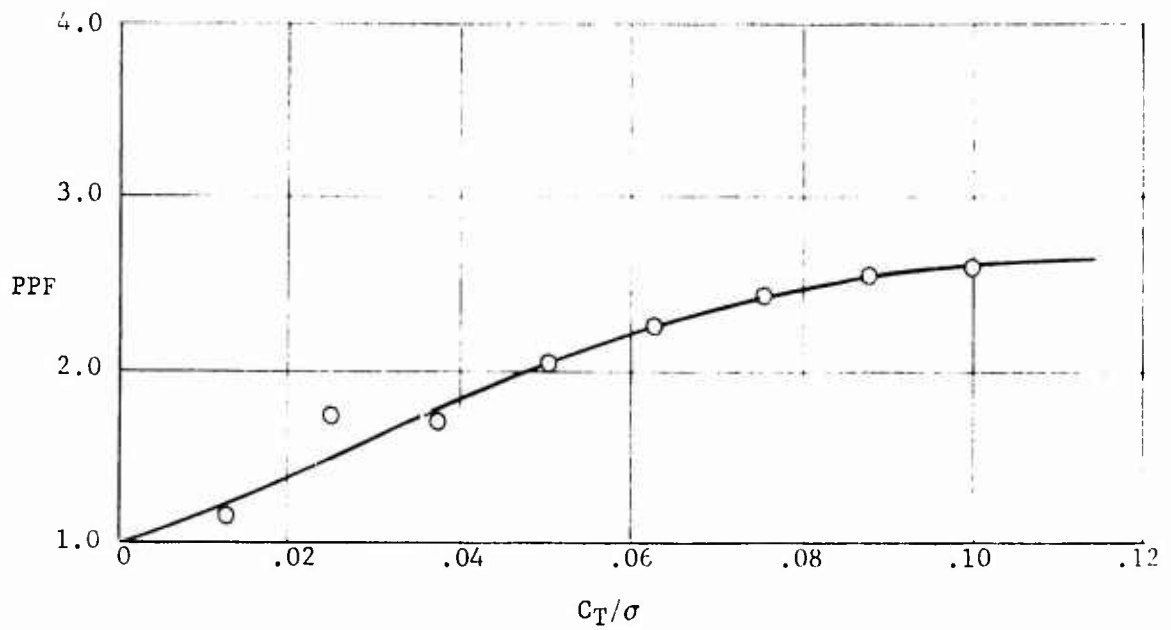
Figure 7. Profile Power Scale Factor, Whirl Test of Reference Rotor

$$PPF = \frac{C_{Q_0} \ (Test)}{C_{Q_0} \ (Theory)}$$

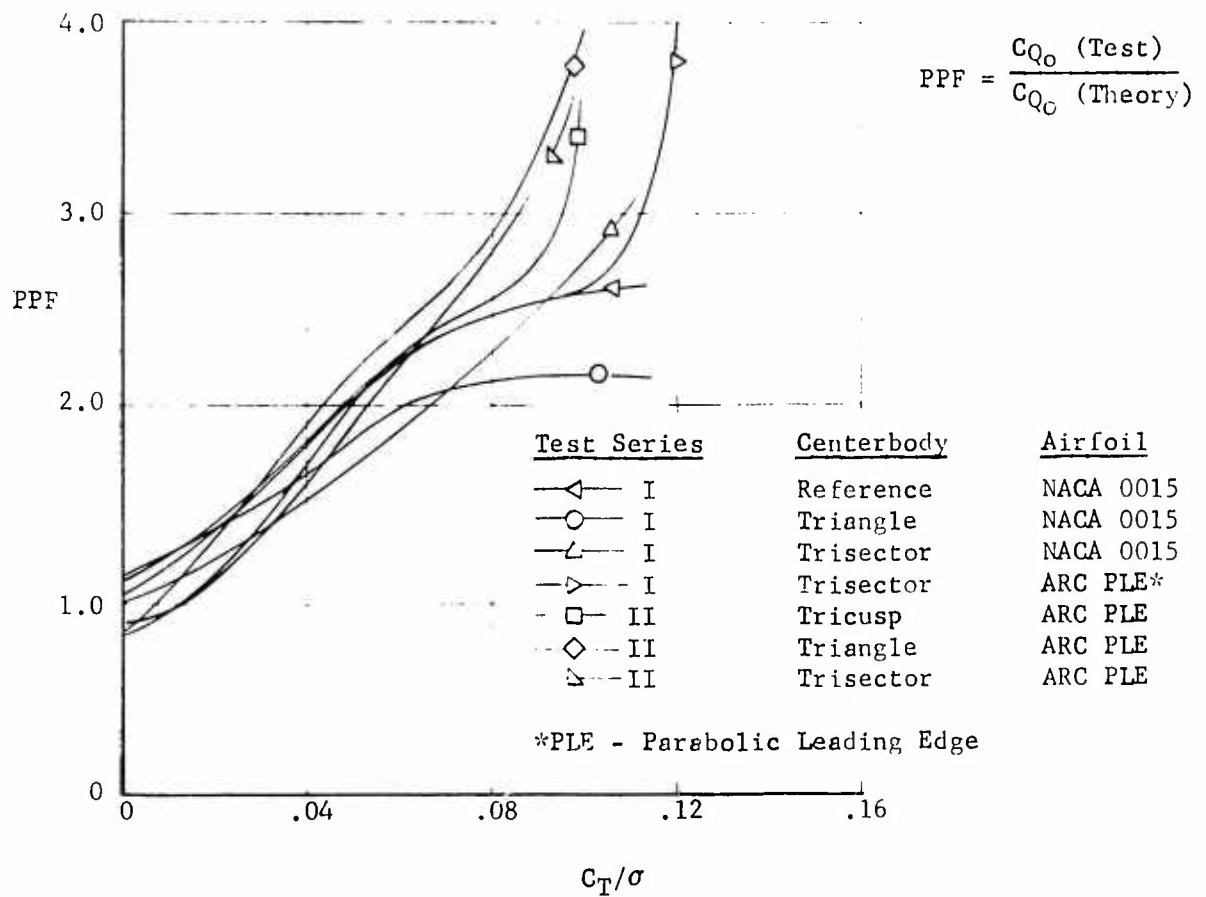| Test Series	Centerbody	Airfoil
I	Reference	NACA 0015
I	Triangle	NACA 0015
I	Trisector	NACA 0015
I	Trisector	ARC PLE*
II	Tricusp	ARC PLE
II	Triangle	ARC PLE
II	Trisector	ARC PLE

*PLE - Parabolic Leading Edge

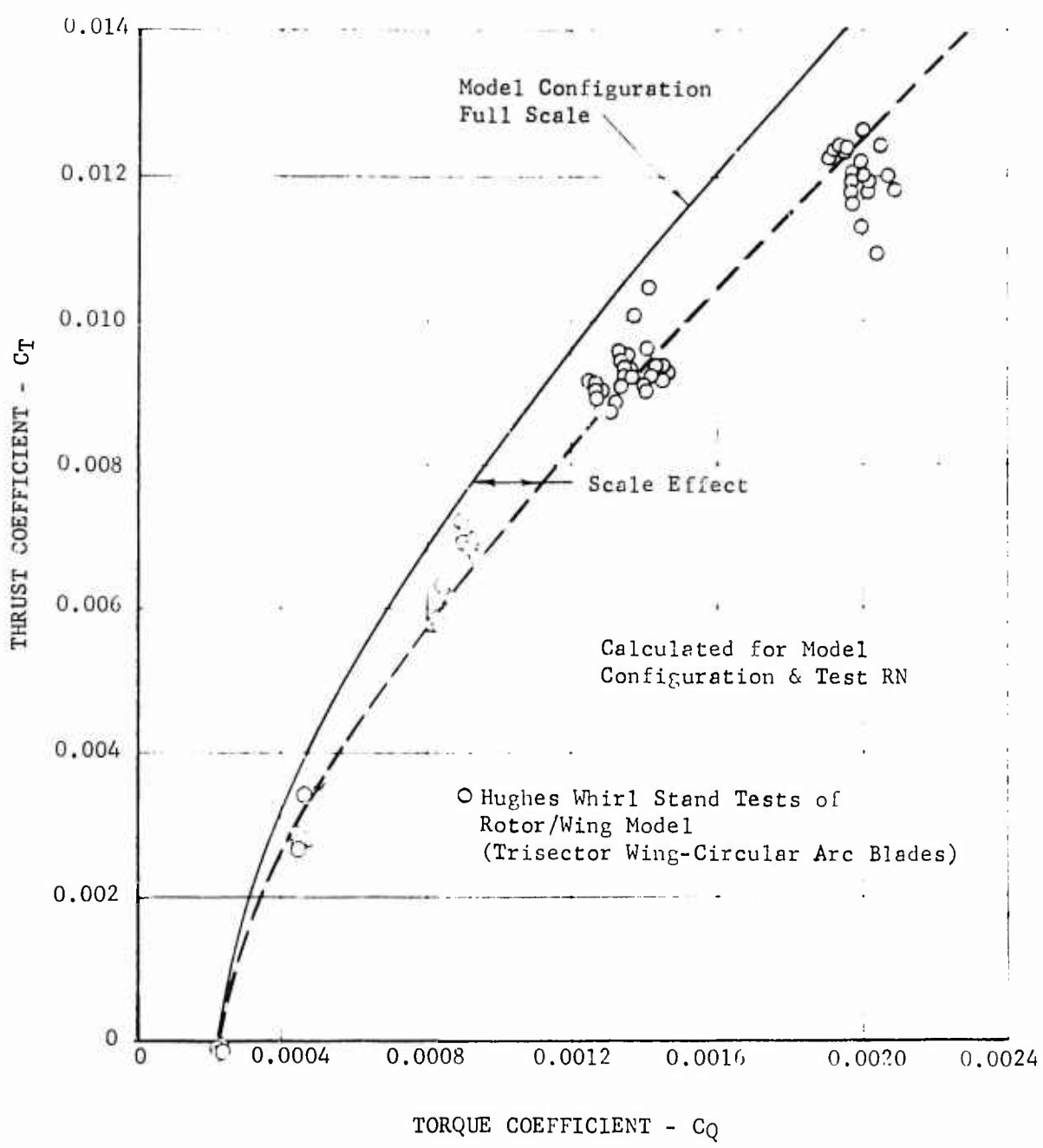Figure 8. Rotor/Wing Profile Power Factor

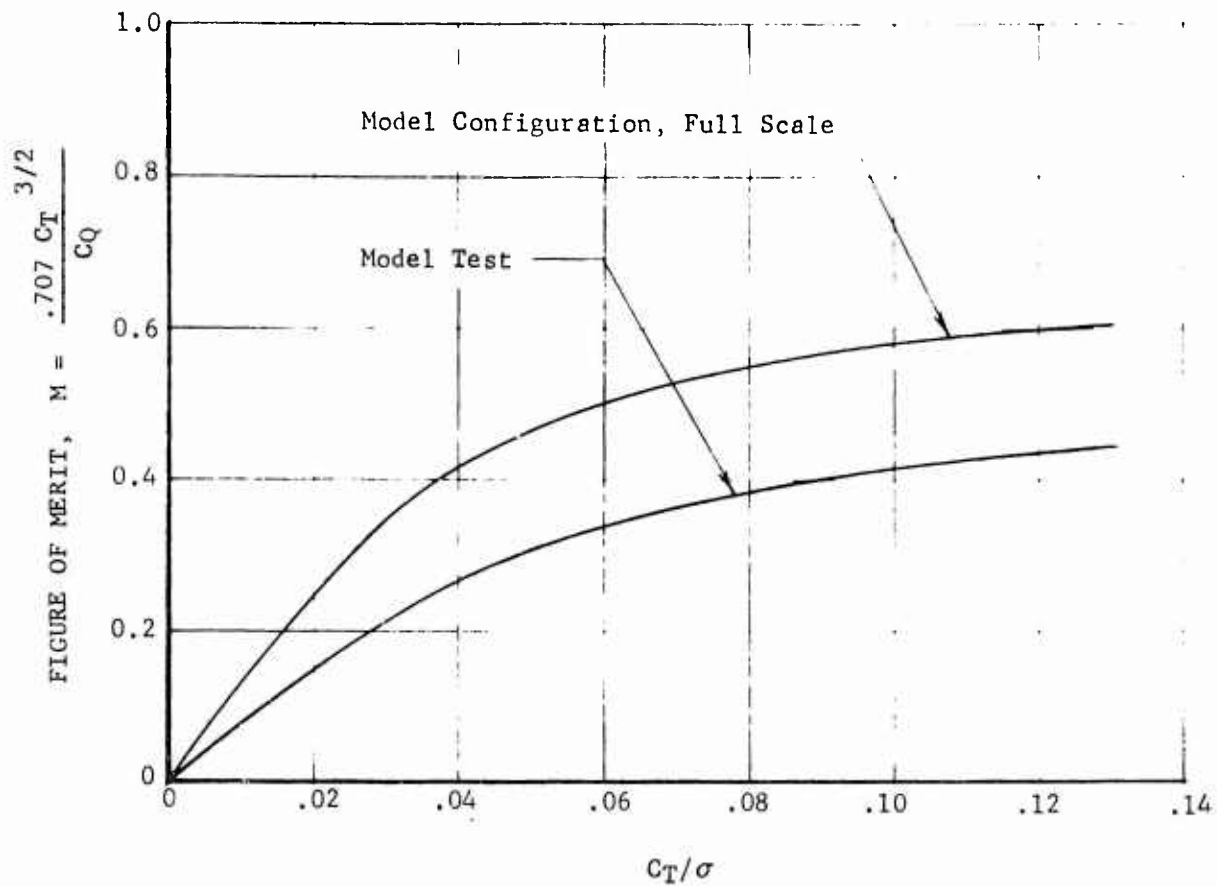Figure 9. Comparison, Rotor/Wing Hover Power and Model Test Data

Figure 10. Rotor/Wing Figure of Merit

AIRPLANE MODE PERFORMANCE - THRUST REQUIRED

The following method of predicting the drag of the Rotor/Wing is based on theory and supported by seven separate wind-tunnel tests of similar configurations in the airplane flight mode. This method is appropriate to the cruise configuration, where the Rotor/Wing is locked to the fuselage with one blade forward, seals and fairings are in place, and the landing gear is retracted. The following equation is appropriate for all speeds between conversion and the beginning of compressibility drag rise:

$$C_D = C_{Do} + \frac{C_L^2}{\pi ARe} + K (C_L^2 - C_{L_B}^2)$$

The first two terms are the classic parasite and induced drag terms. The last term is also an induced drag term typical of highly swept or delta-wing planforms and is associated with the formation of the leading-edge vortex. The following paragraphs describe these terms and their derivation from wind-tunnel test data.

SKIN FRICTION AND FORM DRAG COEFFICIENT

The total drag at zero lift (parasite drag) is the summation of both the skin friction drag associated with aerodynamic shearing force and the pressure or form drag associated with normal forces on the model surface.

The value of the skin friction coefficient depends on the flow condition -- which can be either laminar or turbulent -- on the local Reynolds number, and on the roughness of the skin surface. It has been assumed that the boundary layer will be turbulent on a full-scale vehicle; therefore, the small models tested had roughness strips added to ensure transition from laminar to turbulent conditions during testing. The larger models are believed to have turbulent boundary layers because of their size and the turbulence levels in the wind tunnels where they were tested. Since it is impossible to measure pressure and friction drag separately, the assumption is made that the skin friction coefficient is due to full-turbulent flow at the Reynolds number appropriate to the test conditions and model component. The products of the full-turbulent skin friction coefficient and the wetted area of each component are added together and this summation is divided by total wetted area. The result is the weighted skin friction coefficient shown in the equation below:

$$C_{f_{wtd}} = \frac{C_{f_1} S_1 + C_{f_2} S_2 + \ldots + C_{f_n} S_n}{(S_1 + S_2 + \ldots S_n)}$$

The remaining parasite drag, between that measured and the weighted skin friction, is charged to pressure or form drag. Form drag is not a function of Reynolds number or model scale, but only of model shape and the designer's skill in forming smooth contours that delay separation.

Figure 11 summarizes this discussion, showing the total parasite drag coefficient for several models and test Reynolds numbers. These coefficients are based on wetted area, so the comparison with skin friction coefficients can be made directly. The shaded symbols represent measured test data between $R_n = 10^6$ and 10^7. The open symbols on the turbulent skin friction line from Reference 16 represent that portion of drag assigned as skin friction. The increment between the skin friction line and the test point is due to pressure drag.

The only drag reduction that can be expected between model and full scale is that associated with skin friction. As Reynolds number increases from model size to full-size and velocity increases between the model test conditions and full-scale conditions, the skin friction drag decreases by the schedule shown by the full turbulent line on the figure. Full-scale Rotor/Wing configurations will have skin friction coefficients of approximately 60 percent of the test values.

The apparent wide variations of profile drag, measured during the several tests, is due to variations in configuration. For example, the high drag shown for the Series XI dynamic model is due to that model's large projected frontal area. The rotor control mechanism required that the pylon immediately below the rotor center be of outside proportions. Scaled frontal projections of the Rotor/Wing would be more like that indicated by the Series X data points. The upper of these two points represents the current Rotor/Wing configuration with increased pylon height for adequate blade clearance. The profile drag increment amounts to 0.00093 in terms of skin friction coefficient, and this

will be the same increment full-scale. Thus, the Series X configuration, extended to full-scale conditions, will have a parasite drag of 0.00323. Since the full-scale vehicle will have surface imperfections, miscellaneous antennas, and projections not found on the model, the parasite drag is incremented upward 15 percent. The Series-X configuration parasite drag would be 0.00371 for full-scale conditions.

INDUCED DRAG

The second term of the drag equation represents classic induced drag, dependent on the square of the lift coefficient. The efficiency factor "e" is measured from test data plotted as C_D versus C_L^2. Figure 12 shows a summary of these plots from various Rotor/Wing wind-tunnel tests. These curves show the typical sharp break experienced by wings with highly swept leading edges. This "break", or nonlinearity, is caused by the leading-edge vortex system associated with large sweep angles and small leading-edge radii used on the Rotor/Wing. The slopes of the lower portions of these curves are used to measure values of "e". Table II presents these values along with other parameters measured for each of the appropriate test series.

The value of "e", or the slope of the lower portion of the C_D versus C_L^2 curve, curve, depends on both the Reynolds number and the lift-curve slope to aspect ratio relationship. Reference 21 suggests the following equation for this relationship:

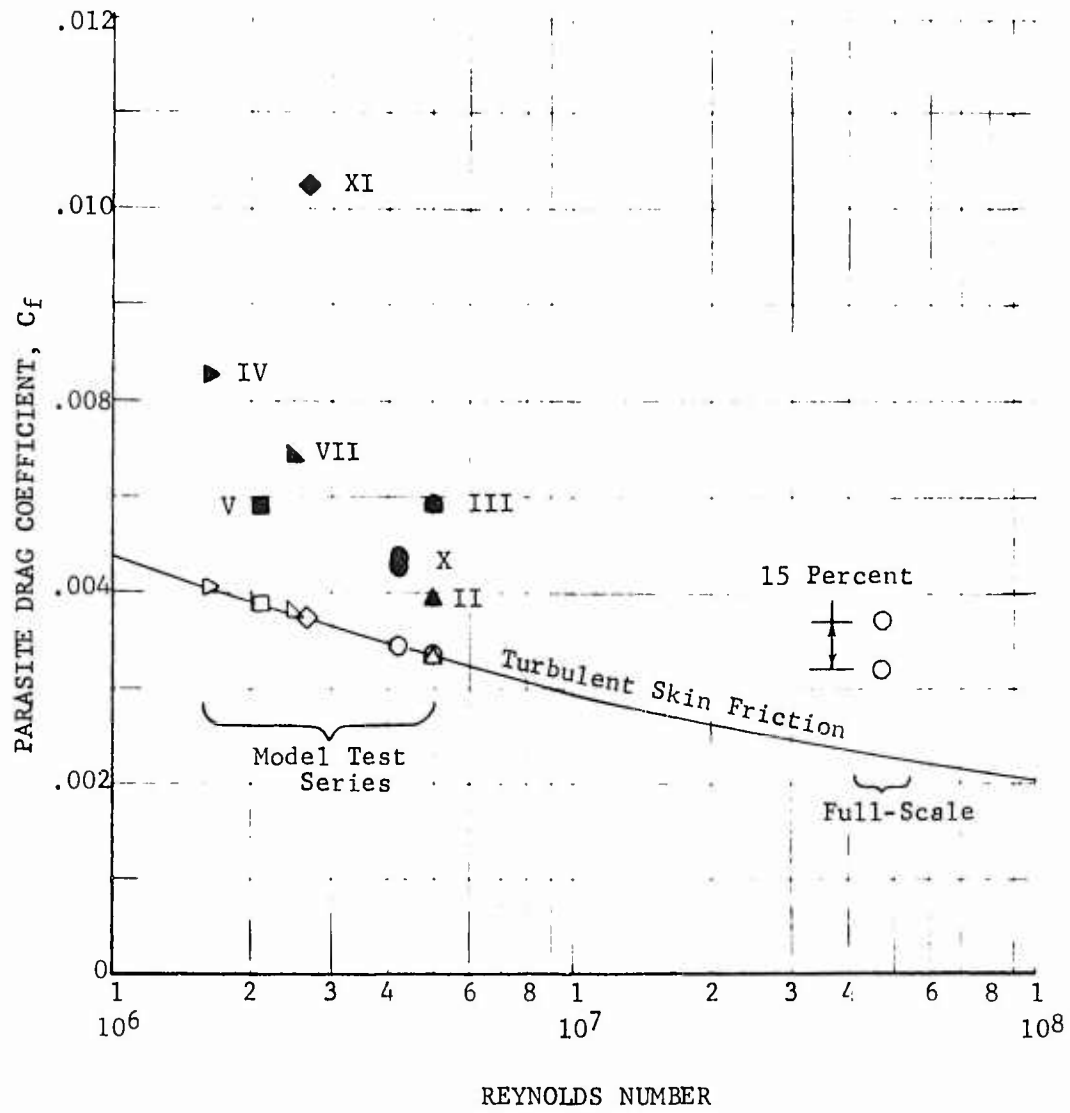$$R = \frac{\dfrac{C_{L_\alpha}}{ARe}}{\dfrac{C_{L_\alpha}}{AR}}$$

Figure 11. Rotor/Wing Parasite Drag Versus Reynolds Number

Table II. Performance Parameter Summary

Test Series	Model Scale	Wing Area	Rotor Area	Wetted Area	Aspect Ratio	Measured Test-Scale (L/D) Maximum	Measured Test-Scale e	Measured Test-Scale R_e Reynolds Number Leading Edge Radius	AR	C_{l_a} per degree	K	C_{l_B}	Full-Scale (L/D) Maximum	Full-Scale e	Full-Scale C_{D_0} *
II	1/7	13.87	40.3	70.8	2.98	9.2	0.68	16.5×10^5	0.96	0.040	0.179	0.356	4.7	0.87	0.0218
III	1/7	13.87	40.3	70.8	2.98	9.2	0.68	16.5×10^5	0.96	0.040	0.151	0.354		0.87	0.0218
IV	1/30	0.73	2.76	4.14	3.96	6.8	0.34	4.5×10^5	0.59	0.052	0.054	0.407	11	0.81	0.0251
V	1/15	3.03	8.73	16.1	3.02	7.2	0.45	9.0×10^5	0.66	0.054	0.238	0.352	10.5	0.84	0.0199
VII	1/15	3.03	8.73	1.8	3.02	7.5	0.58	9.0×10^5	0.76	0.039	0.407	0.343	9.3	0.86	0.0239
X	1/7	10.84	40.3	76.0	3.85	8.6	0.54	18.5×10^5	0.73	0.051	0.055	0.425	10.9	0.86	0.0222
XI	1/7	9.70	40.1	68.8	4.22	6.5	0.72	16.0×10^3	0.89	0.050				0.84	0.0433

Coefficients based on Wing Area

*Does not include 15-percent factor for protuberances and manufacturing irregularities
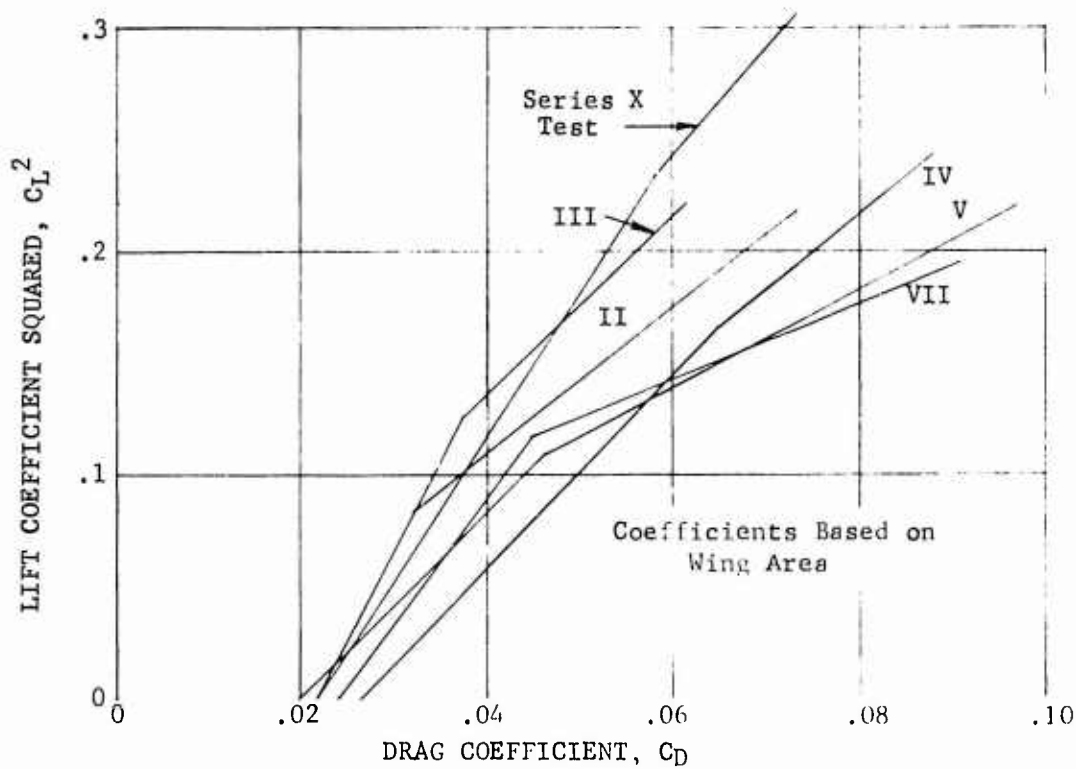

Figure 12. Induced Drag From Several Rotor/Wing Tests

The graph of "R" (Reference 21) plotted against the leading-edge-based Reynolds number shows a large amount of scatter for many reported tests. Figure 13 repeats this plot, without the many data points, and indicates the scatter band of data. The data points shown are for Rotor/Wing tests and, by themselves, show no significant trend with Reynolds number; however, they do lie within the scatter band of data reported. The mean line indicates that a value of R equal to 0.95 can be expected for a full-scale vehicle.

Solving the above equation for "e" and using R = 0.95 and the Series-X measured lift curve slope and aspect ratio leads to full-scale "e" values of 0.84.

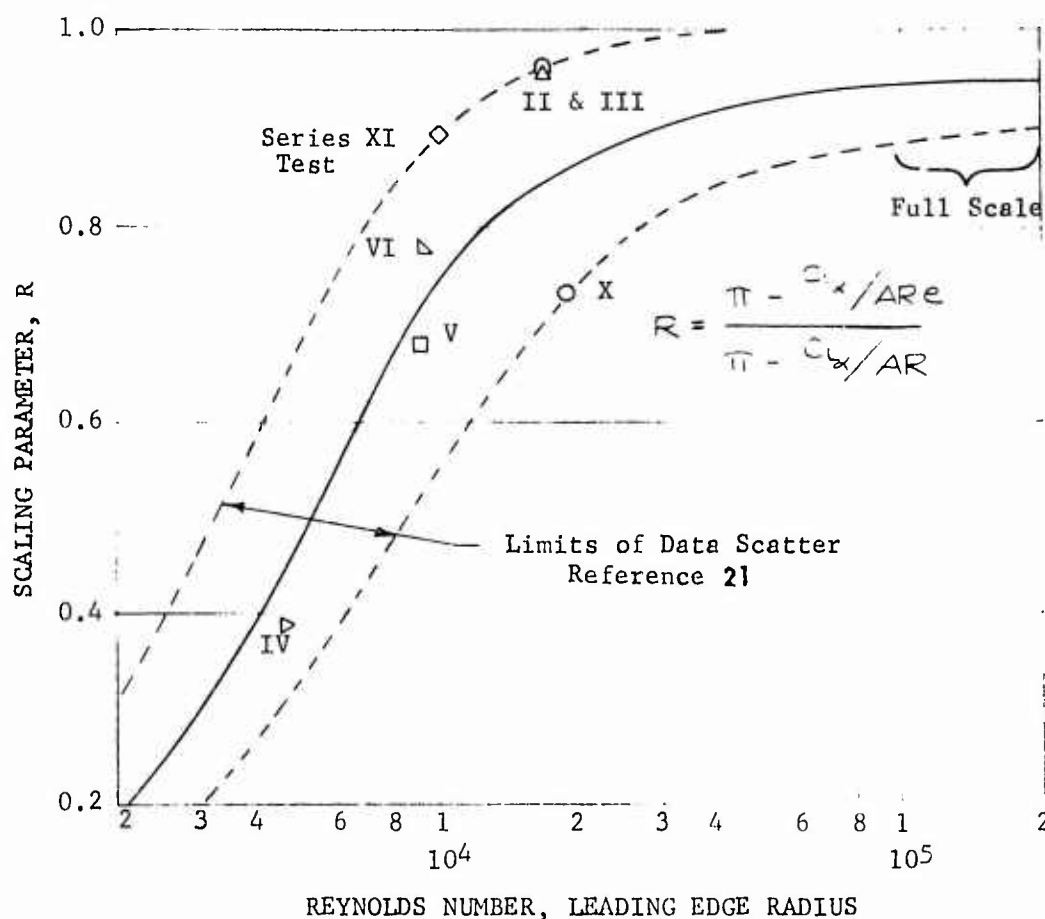$$R = \frac{\pi - c_{l\alpha}/ARe}{\pi - c_{l\alpha}/AR}$$

Figure 13. Induced Drag Scaling Parameter

INDUCED DRAG ASSOCIATED WITH LEADING-EDGE VORTEX FORMATION

The third term in the drag equation applies to operation at high lift coefficients, during low-speed flight, at angles of attack beyond the maximum lift-to-drag ratio. This term accounts for the induced drag in the upper part of the C_D versus C_L^2 lines. Essentially, this K value is empirical and is used to adjust calculated drag polars into agreement with measured polars. As such, no scale factors are applied between model data and the extension to full-scale predicted drag values. Table II also lists these K values.

Figure 14 shows the drag polar computed for a full-scale vehicle that has the Series-X model's geometric characteristics. The maximum lift-to-drag ratio equals 10.0 for the low-speed polar. Also shown on this figure are polars for constant Mach number that show the increased drag associated with compressibility. These high Mach number polars are based on the data obtained from the Series-V transonic tests.

GENERAL

Hover performance, or the rotor power required to hover, and airplane drag, or the thrust required in the airplane mode, were the two primary areas of concern and investigation early in the Rotor/Wing program. The preceding discussion establishes the power requirements for these two flight modes at opposite corners of the operating diagram, Figure 2. The next section discusses the power and thrust requirements along the transition path between these two extreme operation points.

POWER REQUIRED DURING TRANSITION

Figure 15 presents a generalized picture of the power required for steady, unaccelerated, level flight in transition along the schedule of rotor tip-speeds and flight speeds shown on Figure 2. The vertical scale is shown as the
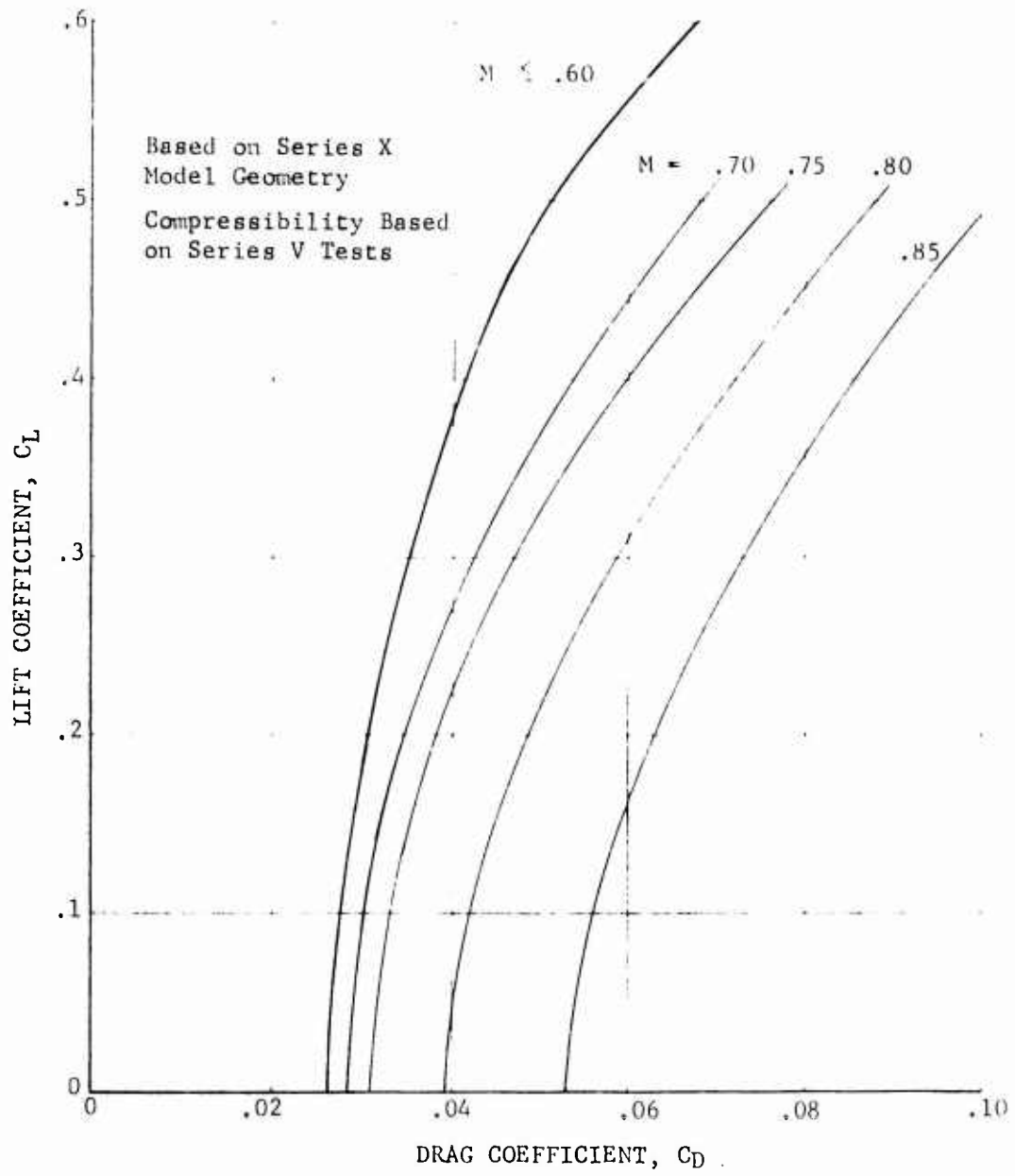
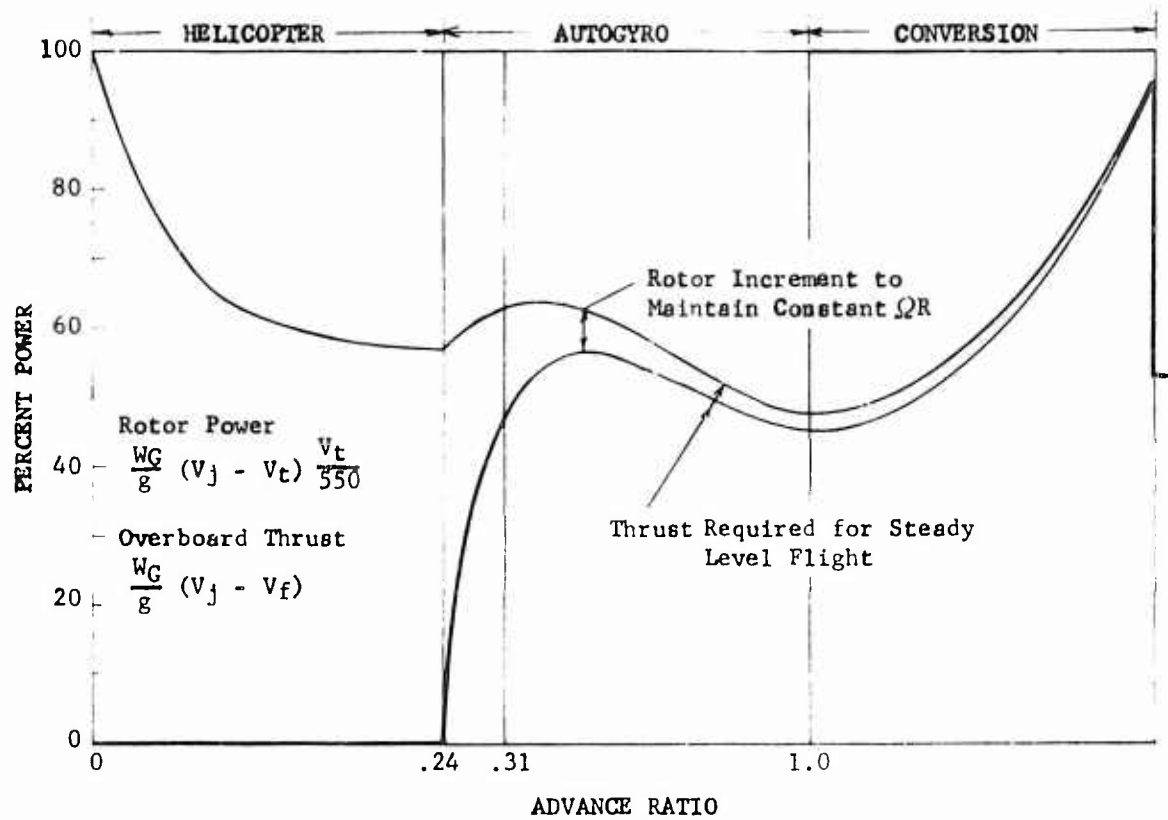Figure 14. Typical Rotor/Wing Drag Polar

Figure 15. Rotor/Wing Power Management in Transition

percentage of gas horsepower required, where 100 percent represents the gas horsepower required to hover. This was done to present a continuous picture of the power required, whether it be rotor power required in the helicopter mode of operation or thrust horsepower in the autogyro, conversion, and airplane modes. The definition of rotor horsepower has rotor speed as a factor, and, when these factors approach zero, the conventional power terms present a misleading view of the true power situation. The horizontal scale is rotor advance ratio, V flight/V tip, running from zero to infinity. Flight speed and rotor speed can be found for any point on the plot by referring back to Figure 2 at the appropriate advance ratio. The operating modes are labeled across the top of the figure and divide the chart into the three separate operating modes.

In helicopter operation, all power or gas flow is directed to the rotor, because the overboard thrust requirement is zero. The details of this rotor-power-required computational procedure are discussed in Reference 8. In summary, this procedure sums the measured blades-off aerodynamic forces and the blade forces given by the NACA performance charts of Reference 22 for advance ratios appropriate to helicopter flight. The charts of Reference 23 are used for higher advance ratios appropriate to autogyro operation. The method of using these charts has been adapted to the Rotor/Wing configuration. Specifically, the adaptation accounts for the following:

1. The lift of the centerbody is subtracted from the total lift provided by the blades

2. The drag increase of the centerbody with angle of attack is included

3. The induced power of the blades is adjusted for the large cutout of the centerbody

4. The rotating torque of the centerbody is included in the analysis.

Currently, the blades-off data was that measured during the Series-X tests, Reference 10, and shown in Figure 16.

Figure 17 presents the comparison of theory and Rotor/Wing model data in rotating-wing, forward-flight mode. For helicopter flight, torque coefficient for theory versus measured data is shown and, for autogyro flight, the total drag coefficient for theory versus measured data is shown. This figure indicates that the theory is capable of matching measured data.

The autogyro mode is initiated by diverting power overboard from the rotor. This accomplishes the step reduction in rotor speed mentioned earlier. Approximately half of the power available is required overboard, and a small increment is required to the rotor to help maintain the rotor speed schedule
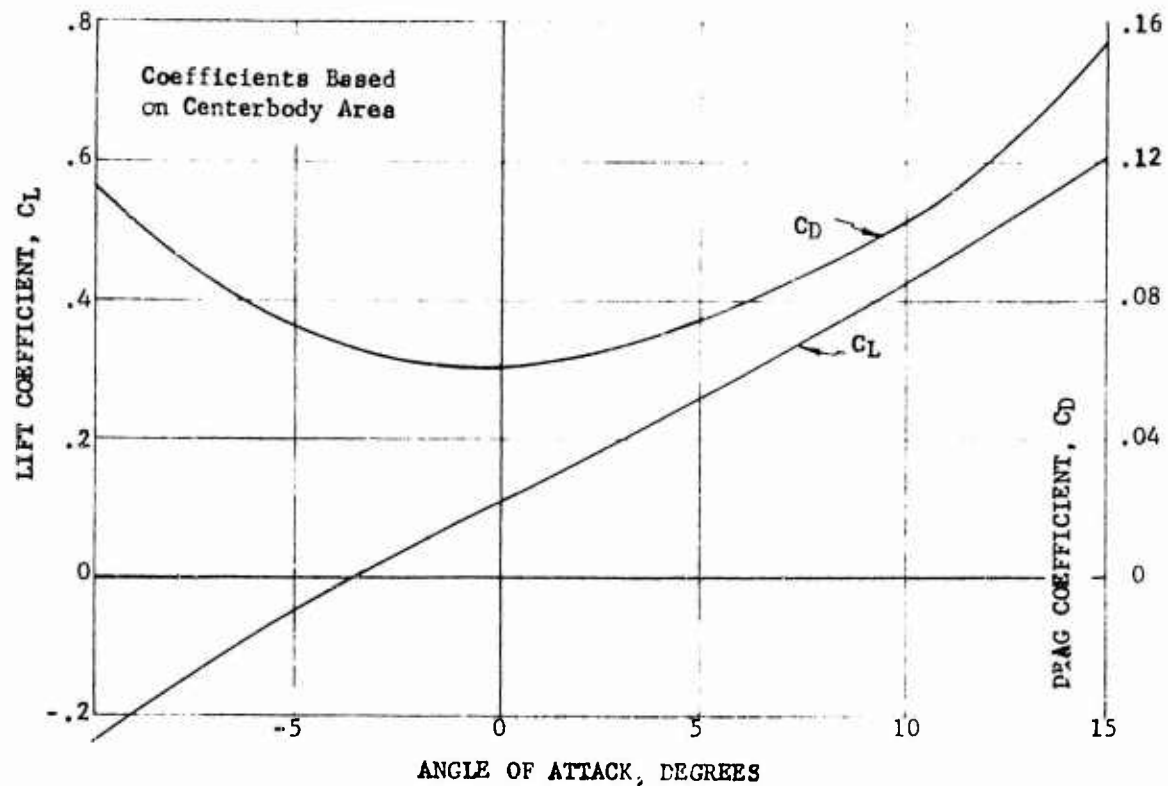
Figure 16. Blades-Off Lift and Drag Characteristics

shown on the operating diagram. The narrow band represents power required
to the rotor to maintain constant rotor speed in both the autogyro and conver-
sion modes. The power margin, above the curve, represents the acceleration
available to the pilot to either accelerate the rotor to proceed to helicopter
operation or to accelerate the aircraft to airplane operation. The right-hand
side of the figure represents another design point to size the engine. Here
the vehicle suffers from the high induced drag associated with blade unloading
and the parasite drag due to open fairings. A small margin, 5 percent, is
left to provide acceleration for maneuver. The initial airplane mode drag is
indicated by the short line at 55 percent power and shows the effect of lower
induced and parasite drag.
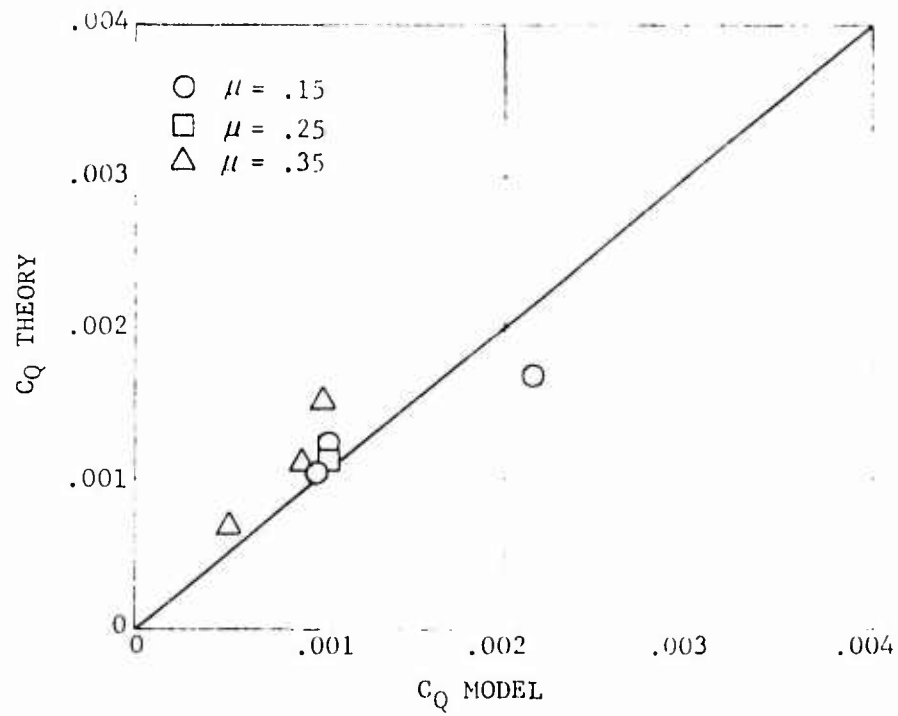
(a) Helicopter Mode
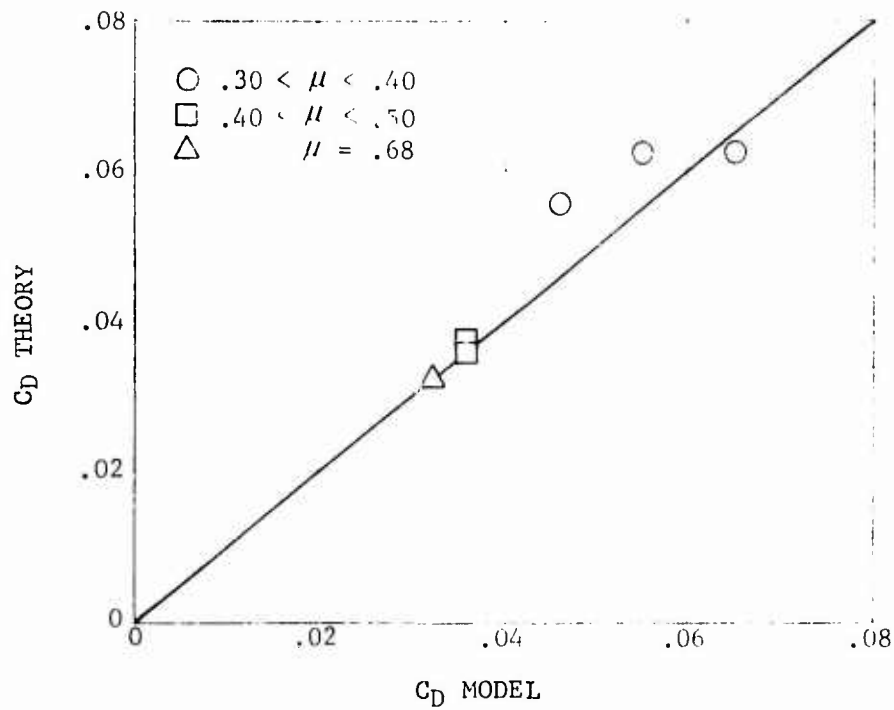
(b) Autogyro Mode

Figure 17.   Theory and Test Data Comparison

The total power picture shows the typical power bucket that is expected for VTOL types in going from powered lift to aerodynamic lift. At the full design gross weight, the ship could fly on one engine in most portions of the diagram. Transition to the helicopter mode could be made on one engine in the event of single-engine failure. Level flight as a helicopter could be maintained at reduced gross weight.

STATIC STABILITY AND CONTROL

It is difficult to present stability and control information separate from performance data, since the calculations and parameters are so interrelated. For example, the blade control angles and angle of attack for rotor-turning operation are obtained as fallout from the performance calculation iteration process using the NACA charts mentioned in the preceding paragraphs. The static stability deficiency mentioned in the opening paragraph of this technical discussion certainly has an influence on the performance capability during transition.

During the high-speed testing of the airplane mode configuration (Series V tests) it was found that stability was lost (both lateral and directional) at high angles of attack. The problem was attributed to leading-edge vortex formation, typical of configurations with large sweep angles on the leading edge. The Series-VII tests, Reference 4, tried several axes; the most promising and straightforward was to increase the vertical tail height and area to maintain stability to a higher angle of attack. This involves setting a maximum or limiting angle for operation.

The maximum angle of attack was set at 10 degrees for normal operation, so, to provide a safety margin, the vertical tail was sized to provide neutral (zero) directional stability at $\alpha - 15$ degrees. Figure 18 shows the critical directional stability parameter, C_{N_β}, for the current configuration. The roll parameter,
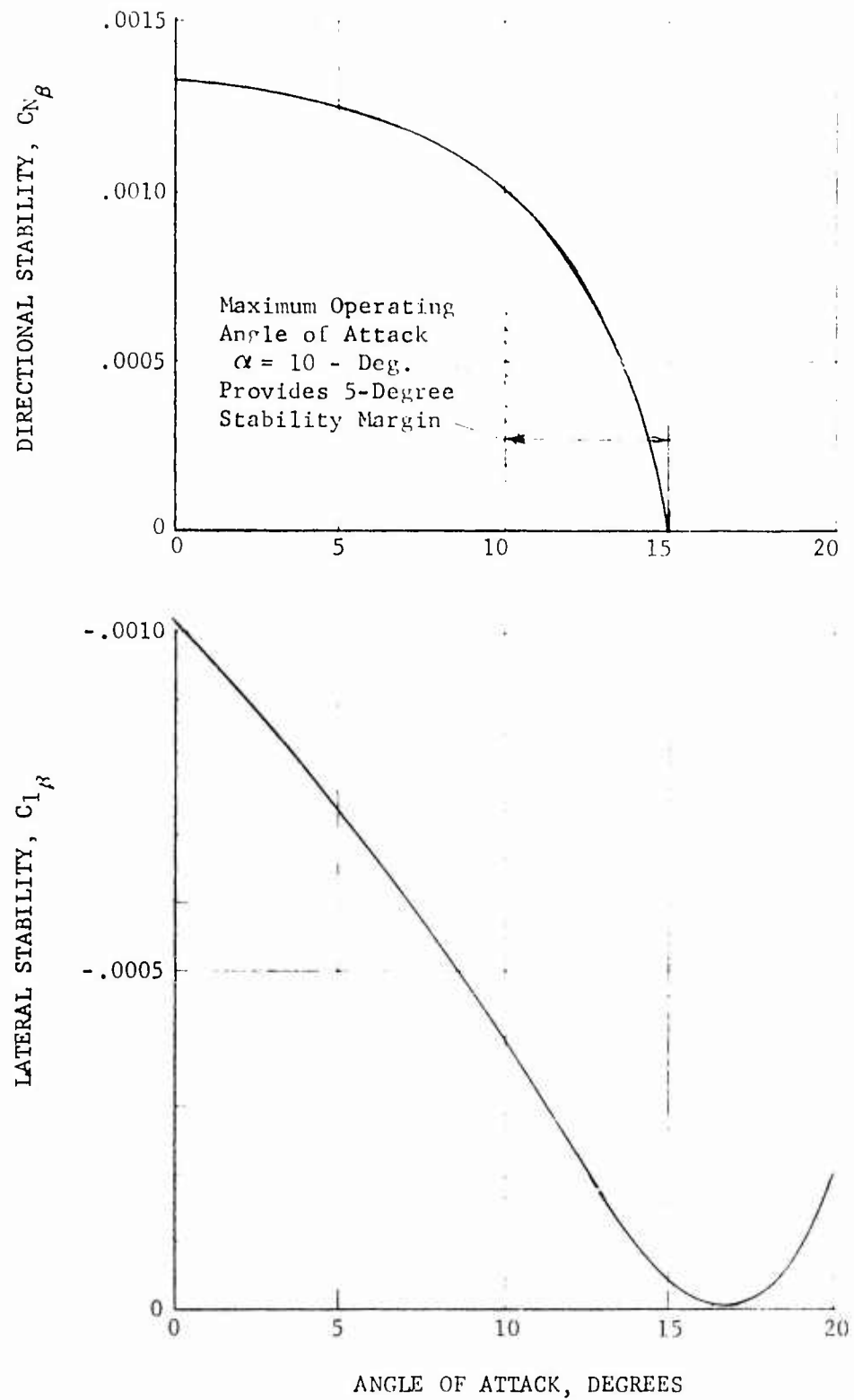
Figure 18. Maximum Operating Angle of Attack

C_{ℓ_β} is not critical, as shown in the lower figure. The data for both figures came directly from the Series-VII tests.

The maximum operating angle of attack (10 degrees) is achieved during conversion (200 knots, $1.0 \le \mu \le \infty$), as shown in Figure 19. The critical point is the upper right-hand corner, where the rotor has just stopped and the blades are still unloaded. As the blades are feathered and begin to sustain aircraft weight, the angle of attack can be lowered. The rest of the α schedule is well removed from the critical area; helicopter flight is characterized by the typical nose-down attitude. The large increase in α between helicopter and autogyro operation compensates for the decrease in rotor speed mentioned previously.

Figure 20 is a plot of the percentage of aircraft weight supported by the wing and by the blades. In the helicopter regime, the blades must supply more than 1-g lift, because of the download on the wing. Even at the extreme nose-down attitude of helicopter operation, $\alpha = -7.5$ degrees, the wing contributes only approximately 4 percent download because of the low dynamic pressure at 40 knots.

The wing and blades exchange roles during the autogyro mode. The wing is completely loaded, so that the oscillating loads associated with blade lift can be minimized.

CONTROL ANGLES IN TRANSITION

The blade control angles are shown on Figure 21. Collective pitch reaches its peak in hover and follows a decreasing schedule that is required to maintain rotor speed and 1-g lift in conjunction with the angle of attack shown in a previous figure. Similarly, the two cyclic angles follow a logical schedule to the advance ratio of 1.0. Here, both collective and A_1-cyclic pitch are ineffective and set to zero. The B_1-cyclic is effective in reducing taper rev
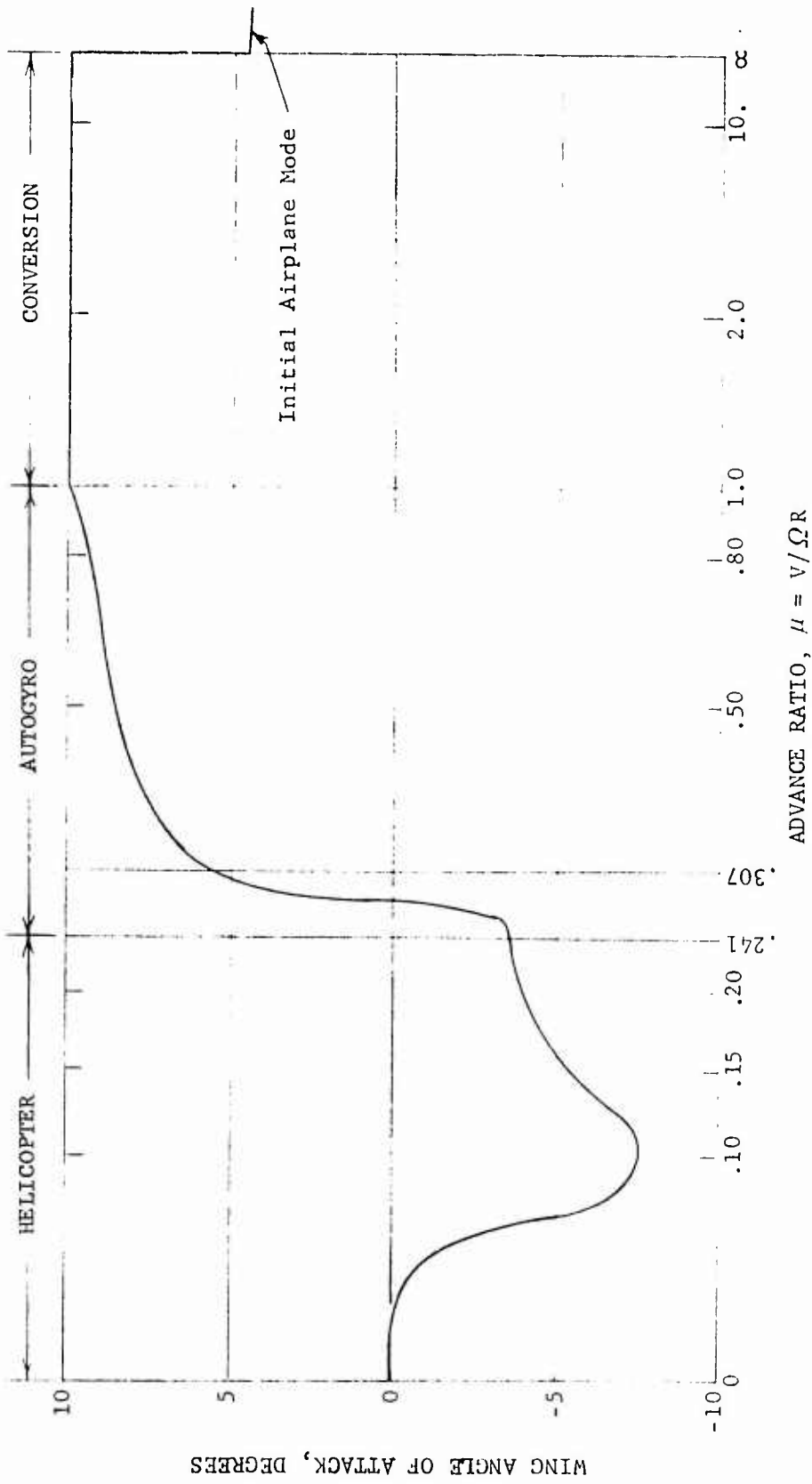
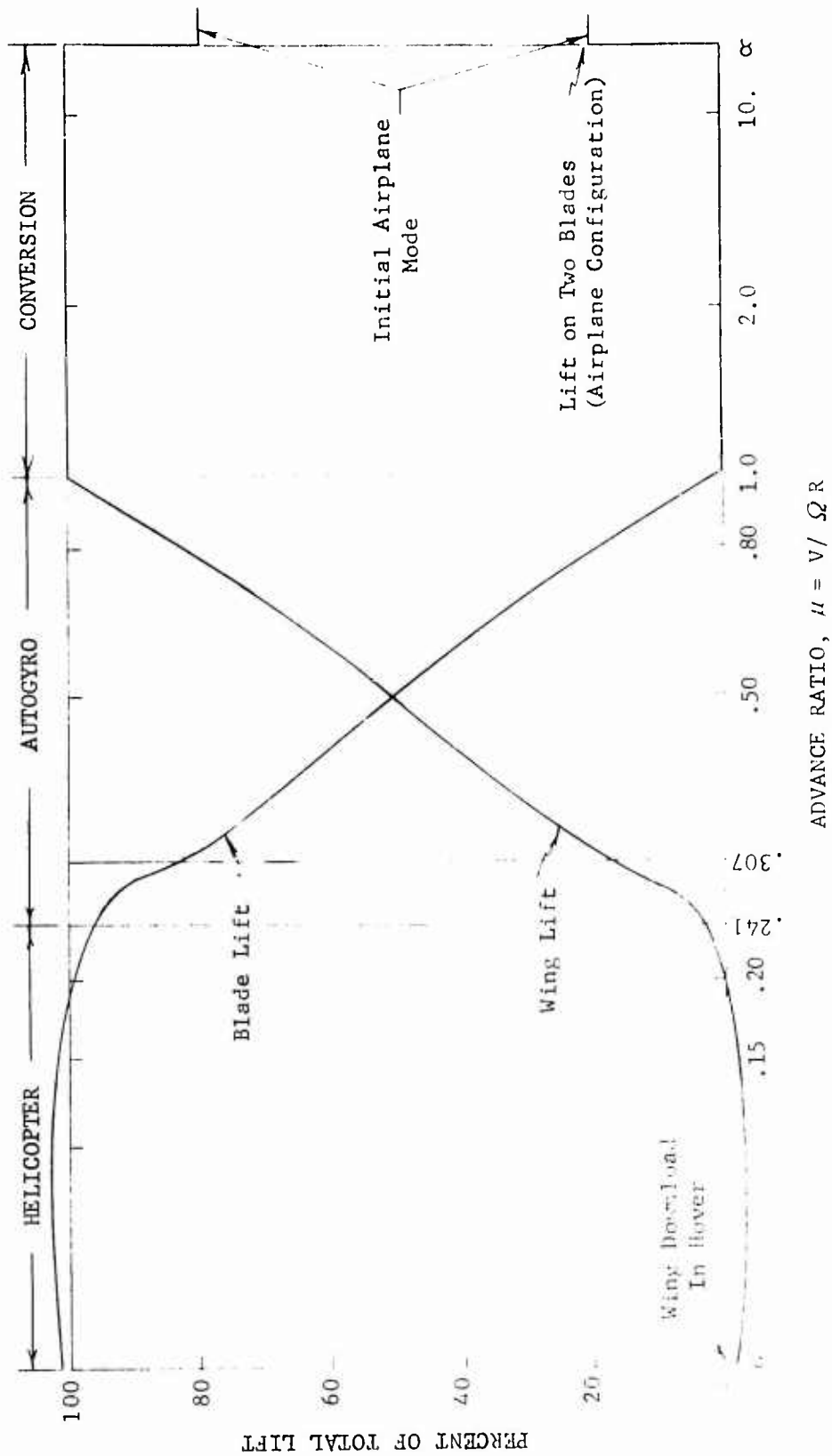Figure 19. Angle of Attack During Transition

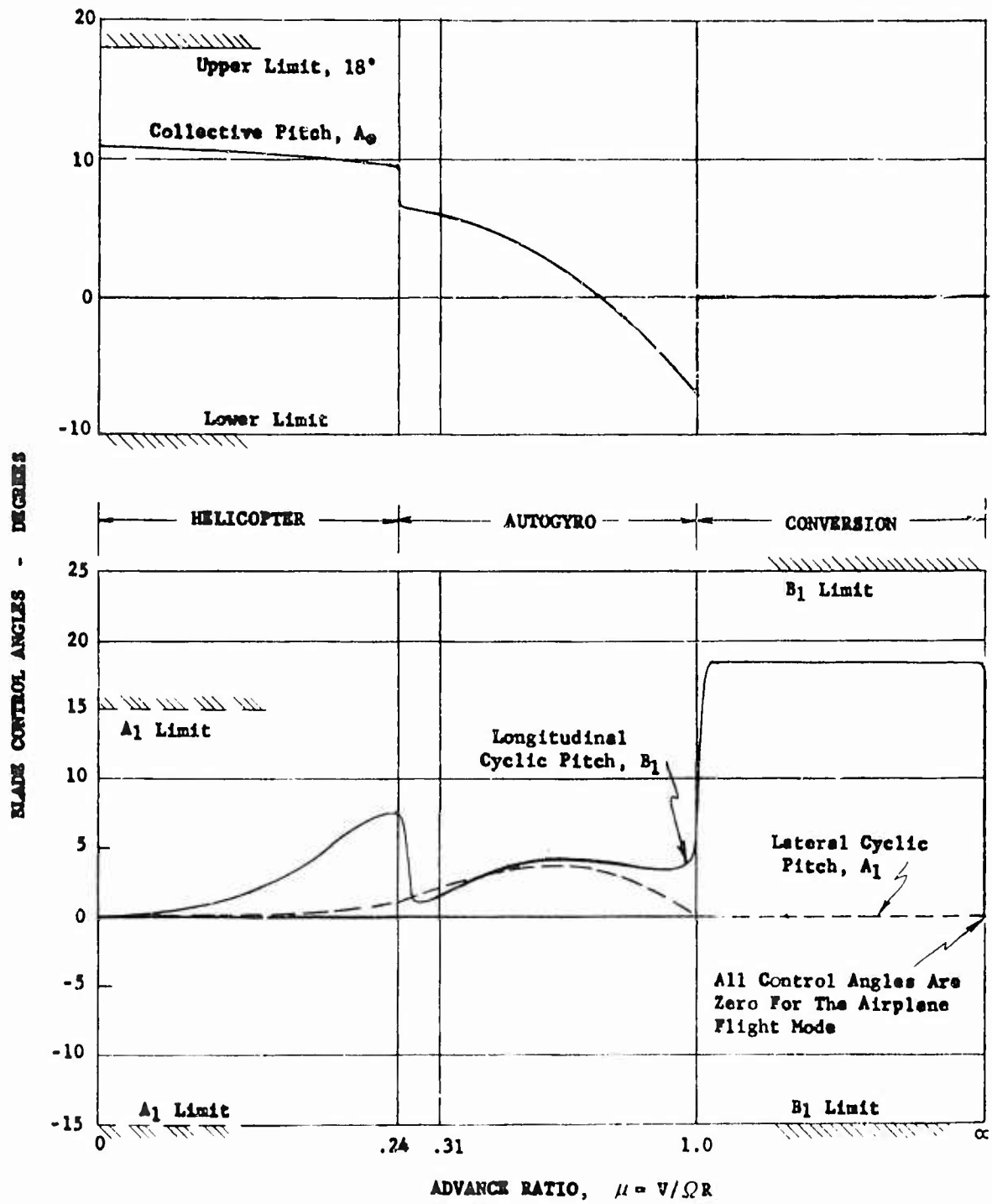Figure 20. Rotor/Wing Blade and Wing Lift Distribution During Transition

Figure 21. Rotor/Wing Control Angles During Transition

pitch and roll moment at the rotor center, if raised to approximately 18 degrees as shown and as discussed later.

GENERAL

Just as stability and control parameters affect aerodynamic performance considerations, aerodynamic loads and structural characteristics also have considerable influence on performance, stability, control, and flying qualities. The operating diagram, shown in Figure 2, is the result of all these considerations. Only the loads imposed on the Rotor/Wing itself are considered in the following discussion; tail loads, landing gear loads, fuselage loads, and so forth, are not discussed. The sketch of Figure 22 shows the orientation and relative location of the various loads discussed, which fall into the two broad categories of static or steady loads and cyclic or oscillatory loads. The subdivision used in this discussion groups the loads that occur at the pylon or rotor shaft together, to be discussed first, and the loads that occur at the blade-root wing-tip junction are discussed second.

PYLON AND ROTOR SHAFT LOADS

One problem discovered early in the Rotor/Wing testing program was associated with the location of the lift vector with respect to the rotor center. On the triangle-shaped centerbody, the lift vector follows an elliptical path that is located somewhat forward of the center of rotation. Not only does the lift vector follow an elliptical path three times per rotor revolution, but the length of the vector varies in the same cyclic manner. This loading system can be resolved into two moments at the rotor center, plus lift, side force, and drag vectors. One of the moments is a once-per-rev rotating beam bending type of loading. It is equal to the moment caused by the lift vector located at the center of the elliptical path, with the rotor turning beneath it. This load does not affect the motion of the aircraft, because it is a steady force balanced by
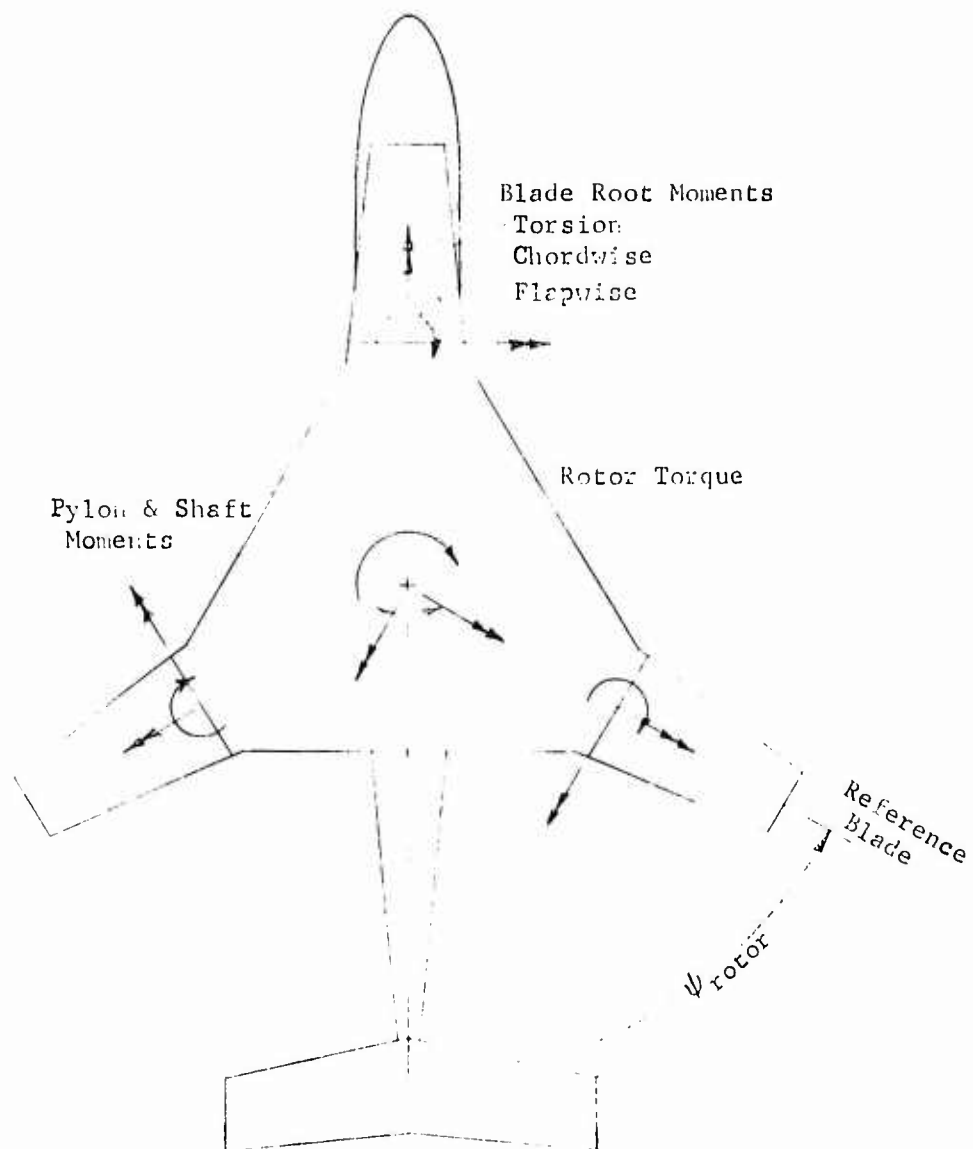
Figure 22. Rotor/Wing Loads Orientation

the tail. It causes only a 1-per-rev cyclic moment in the rotor shaft, which affects endurance loading limits.

One purpose of the Series-X tests was to introduce a cambered centerbody that would move the center of the elliptical path rearward, closer to the rotor center, and reduce this type of loading on the rotor axis. However, the optimum flap arrangement tested, which simulates camber, did not completely eliminate this type of load. The flap arrangement was such that only collective flap deflection was investigated; that is, all three flaps on the wing edges were deflected equally, without respect to rotor azimuth position. It is possible that cyclic variation of flap deflection would shift the center of pressure aft to the rotor center.

In a practical design sense, the cyclic flap mechanism would be similar to a helicopter swashplate, and the structural benefits of reduced loading must be evaluated against the increased weight and complexity of this mechanism. The same is true of collective flap deflection as tested. The benefits of the reduced structural loading must be evaluated against the additional weight and complexity of the flap system. Preliminary analysis indicates that the weight of a flap system will be greater than any structural weight saving accrued through reduced loadings of the rotor mounting structure, relative to a wing with fixed camber.

The second loading type that occurs at the rotor axis is the oscillatory moments, which are primarily at the 3-per-rev frequency in the stationary reference system. These are the "higher order terms" of the series expansion, resolved into the stationary pitch and roll axis system. As an aid to visualizing these loads, consider a circular centerbody without blades. The 1-per-rev rotating beam bending load would be present on the rotor shaft, but all higher order terms would be absent. When the centerbody shape is made triangular, the 1-per-rev is still present (zero-per-rev in the stationary

system), with a 3-per-rev moment superimposed. Similarly, a square centerbody will introduce a 4-per-rev moment in the stationary system. These loads will introduce motion into the aircraft if they are not compensated in some way. Of course, adding blades to the circular centerbody will also introduce these cyclic moments. The introduction of blade cyclic pitch, B_1, is effective in reducing both the 3-per-rev pitch and the 3-per-rev roll oscillations. However, while either of these modes may be made zero by proper choice of B_1 with angle of attack, both modes cannot be zero together. A compromise schedule of B_1 with α has been made to minimize both modes in the ratio of 10 to 1. The resulting pitch moment is 10 times the roll moment; the 10-to-1 ratio is based on the aircraft's relative inertias about the pitch and roll axes. The compromise schedule results in near zero roll moment oscillation and minimum pitch moment oscillation when compared with the $B_1 = 0$ case.

These moments are compared on Figure 23, where the data are from Figures 26, 27, and 31 of Reference 10. These data represent a flaps-on case, no tail on the model, and therefore are not truly representative. However, the large reduction in cyclic moments at the rotor shaft due to application of B_1 cyclic pitch is apparent.

In effect, B_1-cyclic pitch, when used to minimize cyclic shaft loads, is unloading the blades when they are in the lateral quadrants of the rotor disc. Positive B_1 causes a nose-down pitch change with respect to the relative wind, thus the blades are unloaded or possibly down loaded. As a result, mean or average lift is reduced, and to maintain 1-g lift, the angle of attack must be increased. Figure 24 presents the comparison of mean lift from the Series-X test case, where all control angles are zero, with the case where B_1-cyclic pitch follows the angle of attack schedule presented on Figure 30, Reference 10.
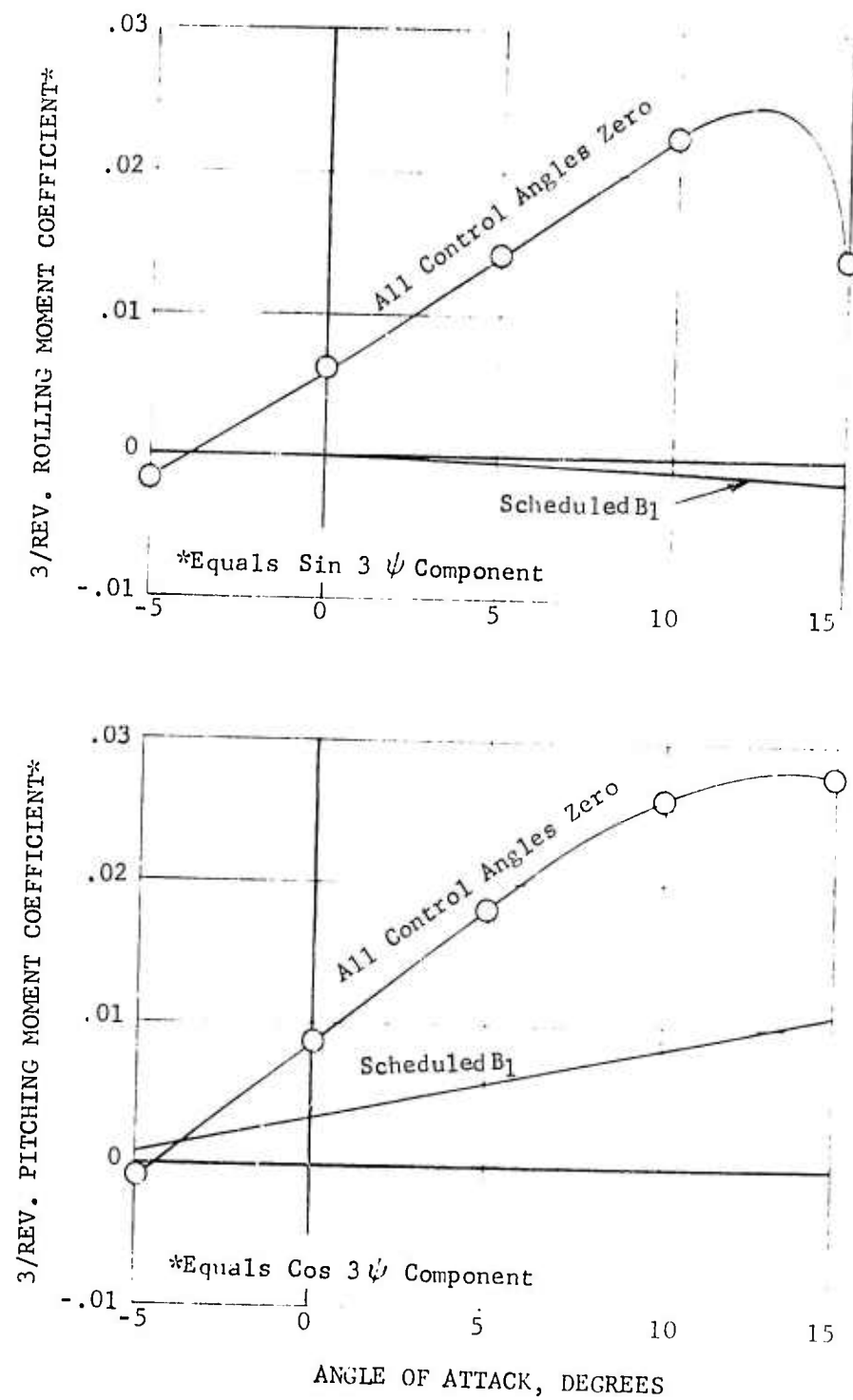
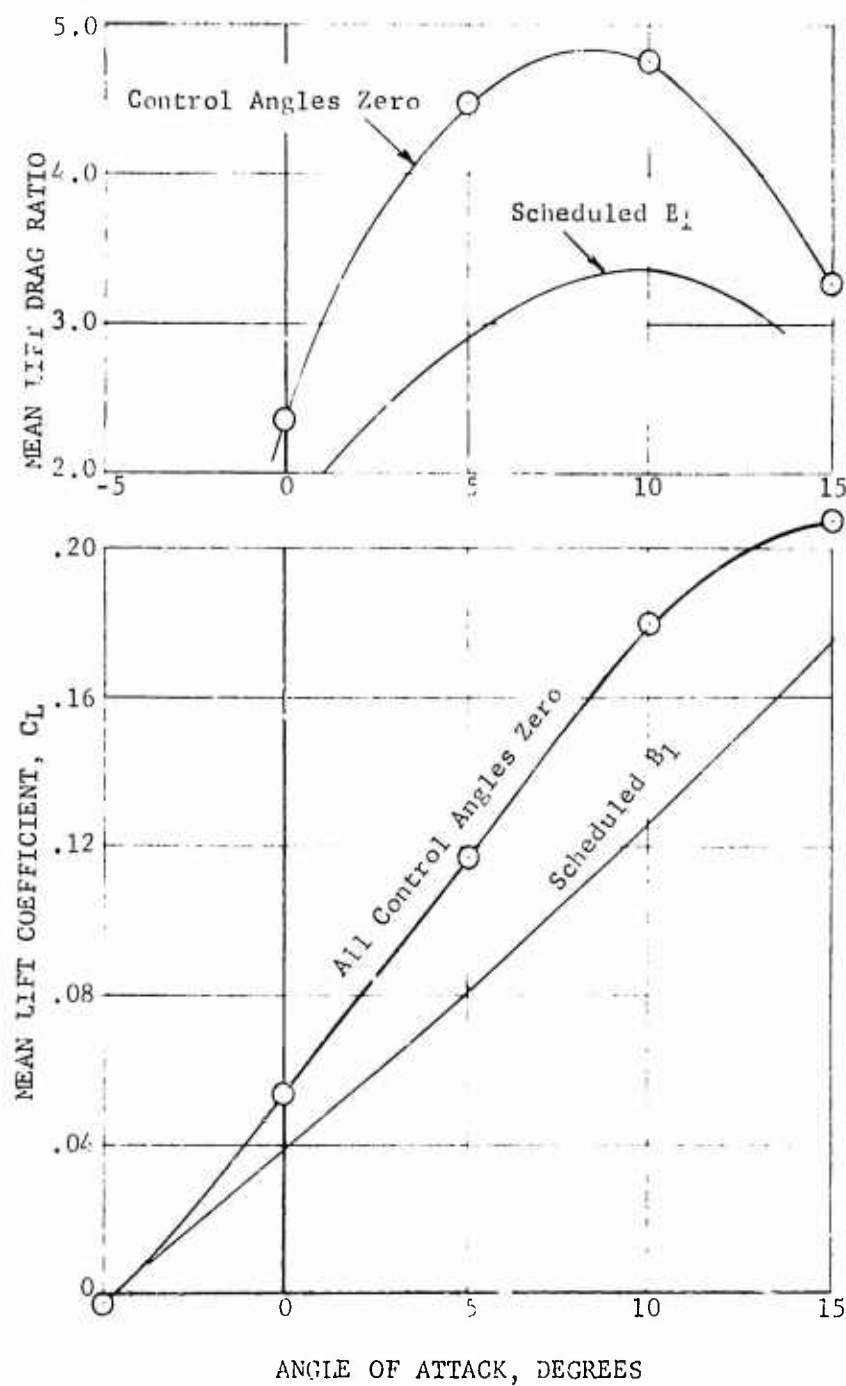Figure 23. Cyclic Shaft Moment Reduction Due to B_1 Cyclic Pitch

Figure 24. Mean Lift Reduction Due to B_1-Cyclic Pitch and the Reduced Lift to Drag Ratio

In addition to the reduced lift, the mean lift-to-drag ratio is reduced as a result of B_1 unloading the blades. The maximum L_0/D_0 for zero cyclic pitch is 4.80 for the configurations as tested. This is reduced to 3.4 as shown in Figure 24. Both of these values will be reduced slightly for the tail-on trimmed condition where a tail-up load is required to balance the static nose-up pitching moment of the Rotor/Wing and fuselage beyond a 4 degrees. This L_0/D_0 reduction, due to blade unloading, is significant in that the installed power must be increased to match this increased drag and maintain an adequate power margin during the conversion maneuver. This is the situation that causes the increased thrust required level at infinite advance ratio shown on Figure 15.

The dynamic model incorporated an adjustably flexible pylon support. This feature provides a very soft pylon (up to a limited amplitude — approximately 3 degrees) to minimize rotor vibrations during forward flight at high and intermediate rotor speeds, and a stiff pylon to provide the structural stability required at the lower end of the rotor speed range during conversion. The purpose of pylon flexibility is to reduce the oscillatory pylon loads when B_1-cyclic pitch cannot be used because it introduces a steady control moment at high rotor speeds.

BLADE ROOT-WING TIP LOADS

Design of the blades, centerbody, hub, and pylon components is primarily determined by oscillating (fatigue) load levels, which, in turn, depend on the structural characteristics of the load-carrying members. These dynamic loads, at the blade-root, were estimated at the time of the CRA preliminary design effort, Reference 1. These estimates were based on limited technology with respect to the Rotor/Wing configuration and on Hughes extensive experience in the rotary-wing field. These loads were believed to be realistic at that time.

In order to verify loads that could be applied to a full-scale design, it was considered necessary to establish a dynamic model design that would be sufficiently clear of resonance with integer multiples of rotor speed in the design operating range and that would be free of mechanical or aeroelastic instabilities. An analytical program was therefore instigated to establish an optimum configuration, from a dynamic standpoint, so that resonance and instability could be avoided with the minimum expenditure of weight. An effort was made to tailor the dynamic model to meet these preestablished design parameters. In order to lower the first collective flapwise frequency to approximately 2-per-rev at 100 percent rpm, it was necessary to incorporate a joint flexible in the flapwise direction at the blade root-wing tip juncture. This flexible joint was designed to incorporate coil springs between the one end of the blade torque tube and the wing structure, with chordwise support provided by a slider closely fitted to a bolt concentric with the coil springs. When this design was tested, it was found that the frictional forces on the sliders could not be reduced to acceptable values, and no time was available to attempt a new design. Figure 25 shows the resonance characteristics of the tested configuration relative to the harmonic exciting frequencies. The proximity of the first cyclic mode chordwise frequency to 1-per-rev and of the first collective flapwise mode frequency to 3-per-rev is evident at the design rotor speed. As a result, some limitations on the operating range of this model were imposed, and the loads obtained included an unrealistically high dynamic amplification factor, so that a correction of these measured loads is necessary before they can be applied to a well designed aircraft.

DYNAMIC LOADS ANALYSIS

Without analytical or theoretical verification, the measured model loads are translated into full-scale loads by the following process.

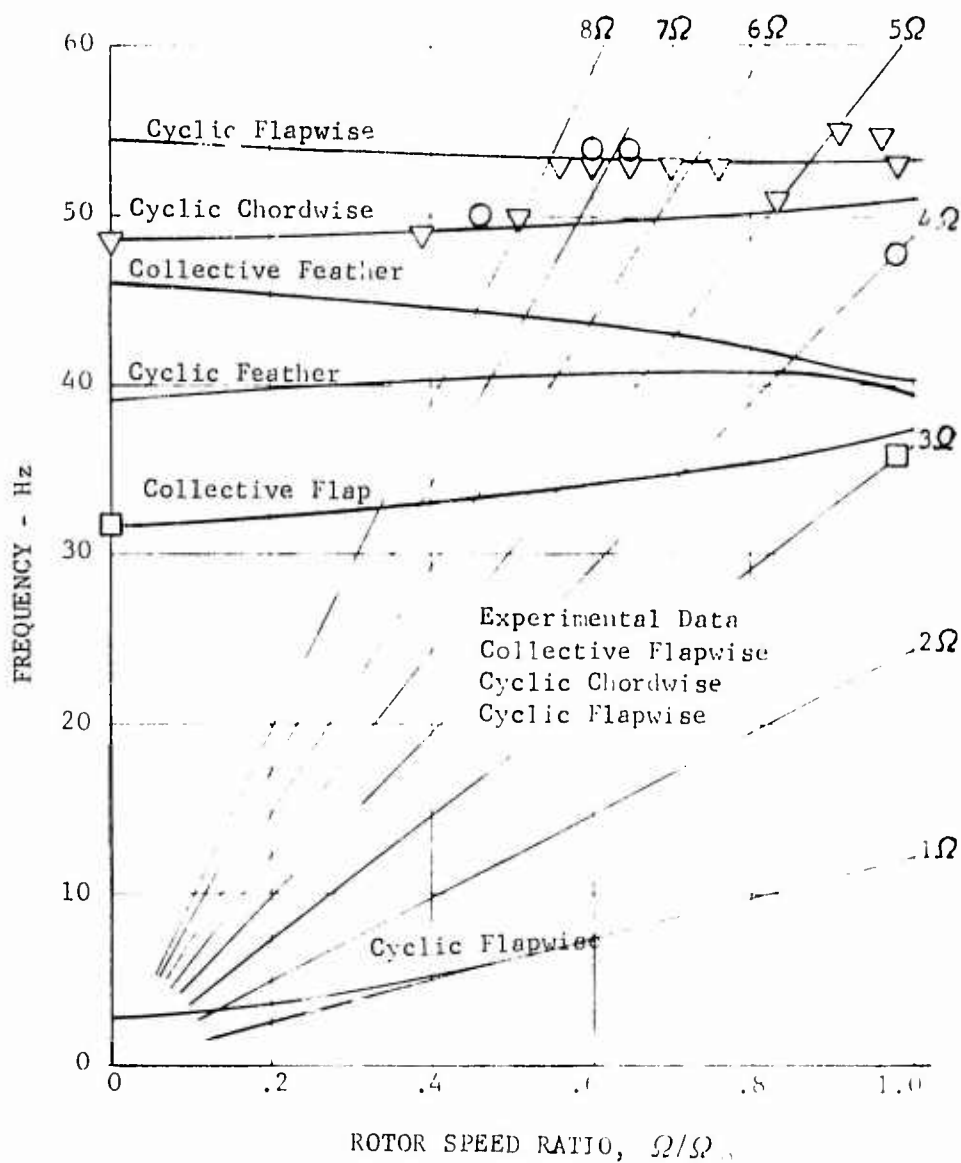Figure 25. Dynamic Model Frequencies, Series XH-1 - 9

The oscillograph records of blade root dynamic loads have been recorded at several advance ratios representing the helicopter and various conversion flight modes. The technique was to read at 30 rotor instants in each of two revolutions for each data point. This data was then analyzed for harmonic components -- the first four being most significant.

A computer program was used to calculate the structural response to an oscillating unit load applied at the 3/4 rotor radius. The frequency of applied load was 1, 2, 3, and 4 times rotor speed for the test data point being considered. The program considered the response of a full-scale type structure and the response of the dynamic model structure. The ratio between these structural responses -- that is, the full-scale type structure to the dynamic model type structure -- has been called a response ratio.

The product of response-ratio and model harmonic moment is the harmonic moment that would be obtained on a model with full-scale structural characteristics. When these products are added vectorially, they represent the overall model moments that would be measured in the wind tunnel if the model had the proper full-scale structural characteristics. Table III shows the response ratio for each of the data point harmonics measured. The lower right shows the vector summation of these ratios to present an overall comparison between model characteristics and full-scale characteristics.

Since the model test data points were not obtained at the "scaled" operating diagram, a small adjustment, usually upward, must be made to the moments on the basis of velocity squared. The final adjustment to the data is made by multiplying by the moment scale factor, which is the linear factor, to the fourth power.

Figures 26, 27, and 28 show the overall blade root moments measured during the Series-XI tests and the four harmonic components extracted from the data. Each of these plots, representing blade-root flapwise, chordwise, and feathering moments, is shown against advance ratio. The left-hand side, up to an advance ratio of 0.25, represents the helicopter mode of operation. The middle of each plot, between advance-ratios of 0.25 and 1.0, represents the autogyro regime. These curves are not continuous, because of the lack of test data between 0.25 and 0.60. The right-hand side represents conversion at 200 knots, following the full-scale operating diagram of Figure 2.

61

Table III. Series XI Dynamic Model Structural Response Ratio

Advance Ratio	Flapwise				Chordwise				Feathering			
	1Ω	2Ω	3Ω	4Ω	1Ω	2Ω	3Ω	4Ω	1Ω	2Ω	3Ω	4Ω
0.16	0.524	0.597	0.071	0.029	1.214	1.835	0.241	0.136	1.312	1.450	0.260	0.200
0.20	0.524	0.597	0.071	0.029	1.214	1.835	0.241	0.136	1.312	1.450	0.260	0.200
0.25	0.524	0.597	0.071	0.029	1.214	1.835	0.241	0.136	1.312	1.450	0.260	0.200
0.57	0.708	1.351	0.369	0.067	0.665	1.771	0.689	0.136	1.180	1.892	0.627	0.294
0.73	0.755	1.415	0.656	0.179	0.452	1.300	1.174	0.344	1.158	1.705	1.025	0.401
0.85	0.796	1.359	1.144	0.297	0.373	1.000	1.527	0.478	1.141	1.524	1.536	0.486
1.02	0.839	1.259	3.134	0.615	0.292	0.714	2.436	0.690	1.130	1.422	2.640	0.575
1.29	0.894	1.147	2.353	1.809	0.199	0.408	1.067	1.464	1.110	1.249	1.890	1.373
2.09	0.937	1.046	1.254	1.805	0.081	0.140	0.230	0.413	1.106	1.120	1.229	1.431
2.52	0.950	1.015	1.156	1.470	0.059	0.096	0.147	0.225	1.105	1.107	1.165	1.273
3.35	0.972	1.000	1.061	1.220	0.035	0.053	0.076	0.105	1.084	1.081	1.103	1.142
6.56	0.994	1.000	1.000	1.031	0.003	0.015	0.019	0.024	1.001	1.073	1.081	1.086

Total Response Ratio (Vector Summation)

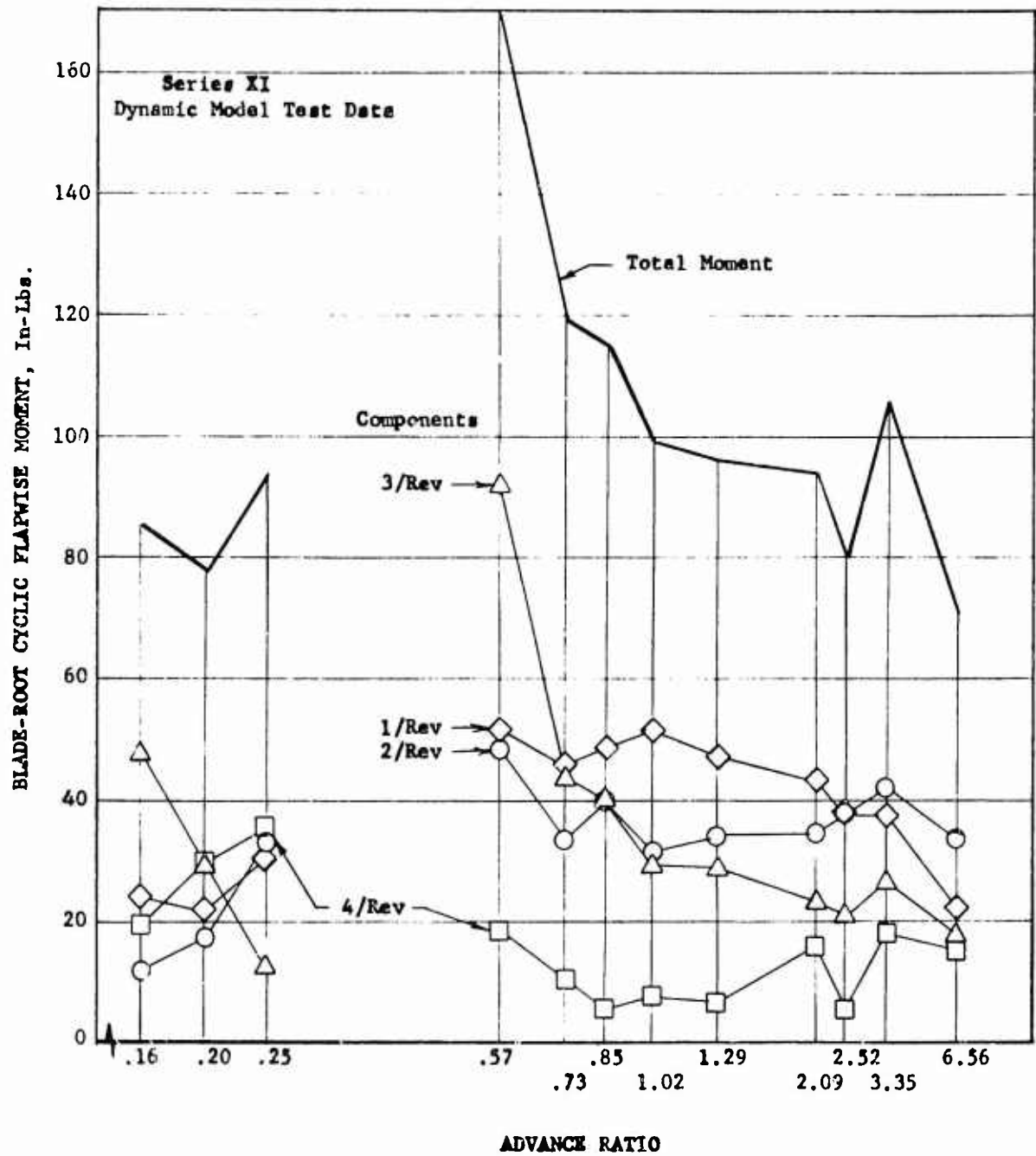| Advance Ratio	Flapwise	Chordwise	Feathering
0.16	0.209	0.526	0.574
0.20	0.238	0.555	0.685
0.25	0.340	0.756	0.816
0.57	0.683	0.825	0.678
0.73	0.768	0.839	0.731
0.85	1.000	0.875	0.978
1.02	1.519	0.852	1.242
1.29	1.383	0.478	1.277
2.09	1.107	0.156	1.143
2.52	1.060	0.104	1.171
3.35	0.925	0.050	0.913
6.56	0.906	0.012	0.903

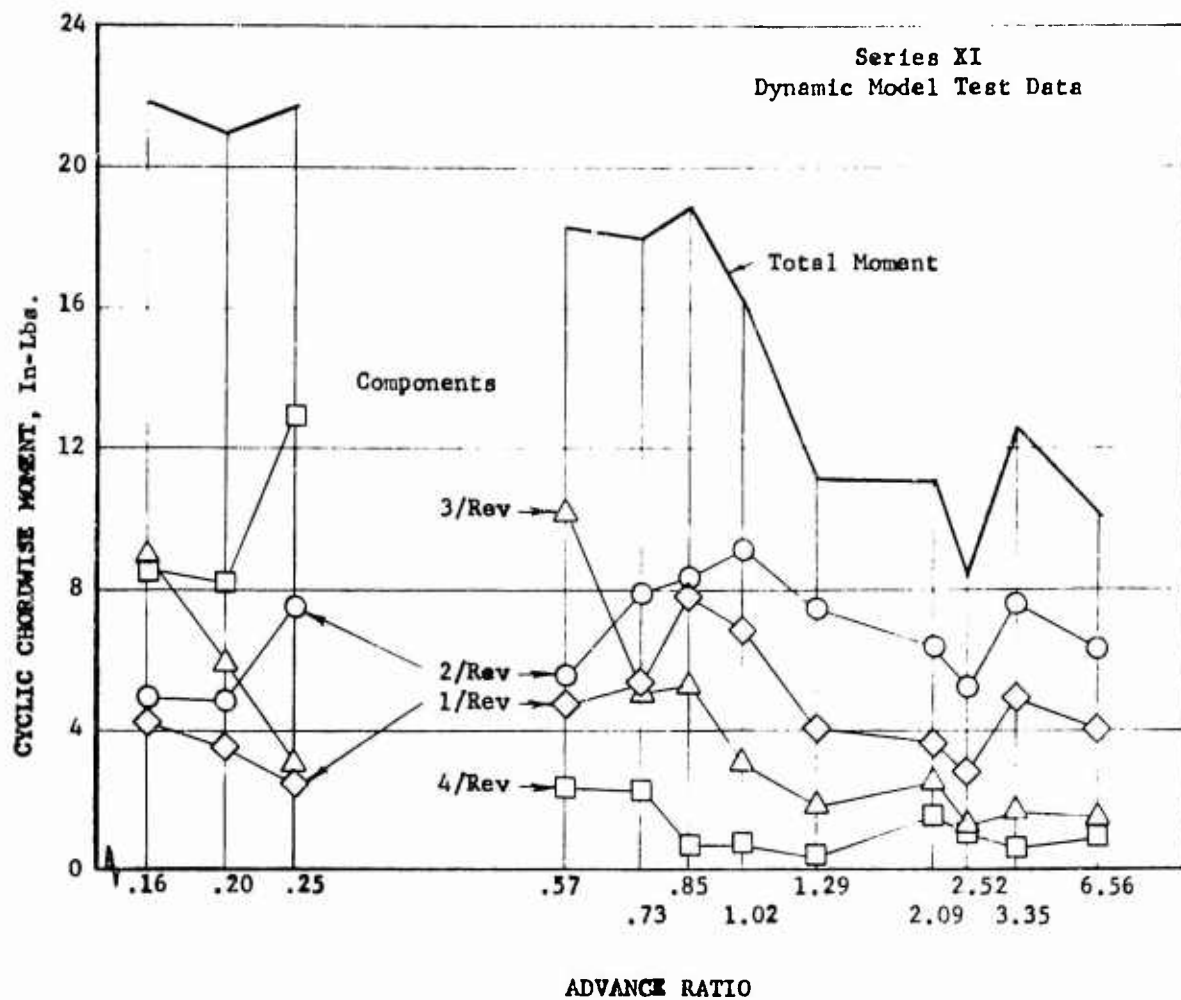Figure 26. Blade-Root Cyclic Flapwise Moment

Figure 27.   Blade-Root Cyclic Chordwise Moment

The cyclic moments shown on Figures 26, 27, and 28 are given in engineering units, because there is no method of presenting meaningful nondimensionalized coefficients for the complete transition path where both rotor speed and flight speed vary from zero to high operating speed. However, these measured loads, when adjusted for scale, response ratio, and operating condition, represent loads considerably higher than anticipated. The flapwise moment reached a level 2.3 times that expected. Similarly, the chordwise moment, Figure 27, is 1.43 times that anticipated. To complete the picture, Figure 28
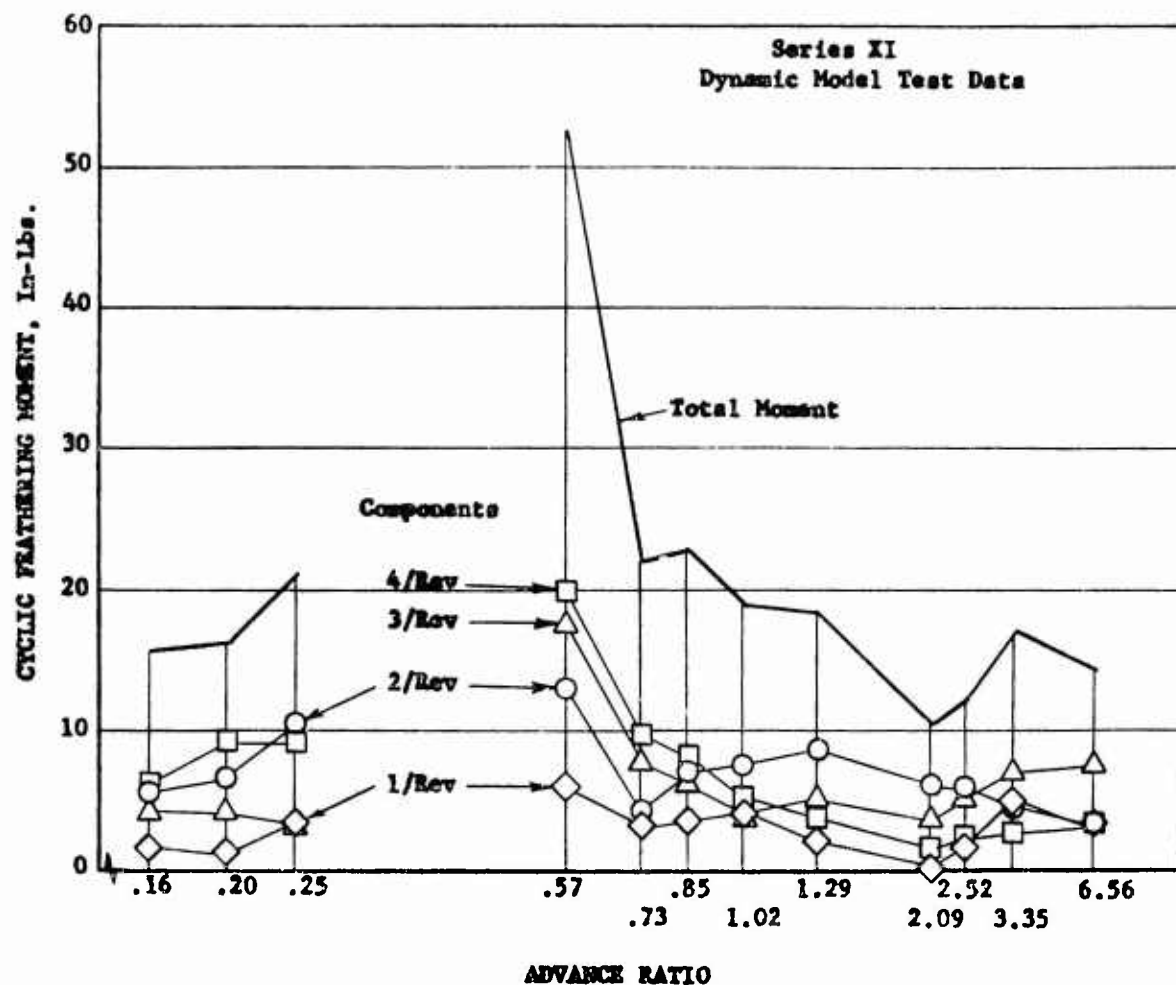
Figure 28. Blade-Root Cyciic Feathering Moment

shows the blade's feathering moment to be 2.75 times the expected level.
Since these levels are so much larger than the anticipated moments, every
effort has been made to verify the test results. Flap bending at $\mu = \tau$ was
checked with another test, Series X, performed earlier, and it verified the
dynamic model data. The data measured on a different blade (Series XI) was
investigated and revealed a similar moment level.

A comparison of blade bending data from the Series-IX tests at an advance
ratio of 0.25 shows some interesting discrepancies. The flapwise oscillating

moment measured during Series XI is approximately 1-1/2 times the value measured earlier. The earlier tests showed considerable scatter, but the majority of data points show levels around ±60 inch per pound at μ = 0.25.

Chordwise bending shows an opposite situation. The earlier tests showed chordwise bending moments of 3 times the values measured during the Series-XI tests. To further confuse the issue, the two tests agree very well with respect to the torsional moment or blade feathering. Thus, of the three components of blade-root bending, the ratios of agreement are 1.5, 0.33, and 1.0 between two tests of very similar models in the same tunnel under close operational conditions.

At this stage, there is no theoretical procedure that will predict these moment levels accurately, and we must rely on test information and results to design blade structural elements, but there seems to be a credibility gap with respect to the test data. For example, the decreasing 3-per-rev component of flapwise bending in the helicopter mode (0.16< μ <0.25) shown on Figure 26 is difficult to believe, especially since the other harmonics are increasing.

Clearly, the question of valid test data must be resolved by a systematic investigation of analysis and further testing.

CONCLUSIONS AND RECOMMENDATIONS

The primary area of concern is now the oscillating or cyclic loads imposed on the Rotor/Wing during the middle region of transition from hover to the stopped-rotor airplane mode. There is no analytical procedure currently available that will predict the load levels measured during the last series of wind-tunnel tests. These load levels are not consistent with an earlier test, Series IX, yet indications are that these measured moments are correct.

The schedule of cyclic pitch and angle of attack developed for the infinite advance ratio situation was used approximately during the high-advance-ratio portions of the dynamic-model tests. This schedule appeared to minimize loads at the rotor center, but it is now thought that this schedule may actually increase the moments at the blade root.

The high cyclic loads represent a potential problem area that occurs in a flight region where the flow field and structural dynamic interactions are extremely complex. It appears that analytical techniques alone are not sufficient to arrive at a solution.

Stability, control, and performance are secondary areas of concern. Aerodynamic performance in the airplane mode can be improved with the existing Rotor/Wing planform shape. Tests of the static rotor in various azimuths show that drag is substantially reduced if one blade faces aft instead of forward in the airplane configuration. The blade-aft rotor position allows an aerodynamically cleaner pylon design, plus it allows a shorter forward fuselage, resulting in an empty weight saving.

A circular-centerbody planform will minimize the 3-per-rev shaft loads introduced by the triangle centerbody tested. The circular shape will also present more planform area for vehicle support during transition. In addition, this shape has slightly better hover performance.

It is recommended that a general program of testing and analysis be conducted in the flight region where high blade loads have been measured so that the techniques required for load prediction can be developed.

REFERENCES

1. Technical Report Hot Cycle Rotor/Wing Composite Research Aircraft, HTC-AD Report 66-1, May 1966

2. F. J. Briardy, Rotor/Wing Series IV Wind Tunnel Test, 1/30-Scale CRA Stopped-Rotor Low-Speed Model, HTC-AD 66-5, Hughes Tool Company - Aircraft Division, Culver City, California, January 1966

3. F. J. Briardy, Rotor/Wing Series V Wind Tunnel Test, 1/15-Scale Transonic Model, HTC-AD 66-9, Hughes Tool Company - Aircraft Division, Culver City, California, September 1966

4. F. J. Briardy, Rotor/Wing Series VII Wind Tunnel Test, 1/15-Scale Lateral/Directional Stability Model, HTC-AD 67-7, Hughes Tool Company - Aircraft Division, Culver City, California, May 1967

5. John T. Matthews, Low Speed Static Stability Tests of a 1/15-Scale Unpowered Rotor/Wing Model Series VII, Aerodynamics Laboratory Test and Evaluation Report, Naval Ship Research and Development Center, Washington, D. C., December 1968. AD-852523

6. J. T. Matthews, Low-Speed Wind-Tunnel Investigation of a Circular and a Triangular Rotor/Wing Model in the Stopped-Rotor Mode, Test Report AL 23, David Taylor Model Basin, October 1965

7. R. E. Head, Summary Technical Report Rotor/Wing Concept Study, HTC-AD 65-15 (Series II and III), Hughes Tool Company - Aircraft Division, Culver City, California, September 1965. AD-473-I 862L, -II 864L, -III 863L

8. F. J. Briardy and R. E. Head, Rotor/Wing Series VI Wind Tunnel Test, 7-Foot Diameter Model in the NASA IRC 30 x 60-Foot Wind Tunnel, HTC-AD 67-3, Hughes Tool Company - Aircraft Division, Culver City, California, March 1967. AD-673964

9. F. J. Briardy and F. S. Okamoto, Rotor/Wing Series VIII Wind Tunnel Tests, Concept Model, High Advance Ratio, HTC-AD 67-49, Hughes Tool Company - Aircraft Division, Culver City, California, September 1967

10. F. J. Briardy, Rotor/Wing Series X Wind Tunnel Tests Concept Model With Wing Flaps, HTC-AD 68-20, Hughes Tool Company - Aircraft Division, Culver City, California, June 1969

11. John T. Matthews, Low-Speed Wind Tunnel Investigation of a Circular and a Triangular Rotor/Wing Model in the Stopped-Rotor Mode, Test Report AL-23, David Taylor Model Basin Aerodynamics Laboratory, Washington, D. C., October 1965

12. Martin L. Cook and Robert A. Wilson, Wind Tunnel Tests of a Rotor/Wing VTOL Aircraft Model - Part I - Original Tail Position, Aerodynamics Laboratory Research and Development Report, Naval Ship Research and Development Center, Washington, D. C., December 1968

13. F. J. Briardy, Rotor/Wing Series 1 Whirlstand Test, HTC-AD 63-40, Hughes Tool Company - Aircraft Division, Culver City, California, May 1963

14. F. J. Briardy, Rotor/Wing Series II Whirlstand Test, 7-Foot-Diameter Model, HTC-AD 66-8, Hughes Tool Company - Aircraft Division, Culver City, California, April 1966

15. Alfred Gessow and Garry Myers, Aerodynamics of the Helicopter, The MacMillan Company, New York, N. Y., 1952

16. Sighard F. Hoerner, Aerodynamic Drag, The Oberbein Press, Dayton, Ohio, 1951

17. James P. Shivers and Paul J. Carpenter, Effects of Compressibility on Rotor Hovering Performance and Synthesized Blade-Section Characteristics Derived From Measured Rotor Performance of Blades Using NACA 0015 Airfoil Tip Sections, NACA TN 4356

18. Paul Carpenter, Effects of Compressibility on the Performance of Two Full-Scale Helicopter Rotors, NACA TN 2277

19. Kenneth R. Reeder, Wind Tunnel Test, at High Advance Ratios, of the Hughes Rotor/Wing Aircraft Model (Series X) With Wing Flaps, Naval Ship Research and Development Center TR AL-65, December 1969. AD 865-743

20. Model Versus Full-Scale Rotor Testing, Proceedings of the Third CAL AVLABS Symposium, Aerodynamics of Rotary Wing and V/STOL Aircraft, Volume II

21. R. C. Frost and R. Rutherford, <u>Subsonic Wing Span Efficiency</u>, AIAA Journal, American Institute of Aeronautics and Astronautics, April 1963

22. A. Gessow and R. Tapscott, <u>Charts for Estimating Performance of High-Performance Helicopters</u>, NACA TN 3323, 1955

23. W. H. Tanner, <u>Charts for Estimating Rotary Wing Performance in Hover and at High Forward Speeds</u>, NACA CR-114, November 1964

DOCUMENT CONTROL DATA - R & D

(Security classification of title, body of abstract and indexing annotation must be entered when the overall report is classified)

1. ORIGINATING ACTIVITY *(Corporate author)*	2a. REPORT SECURITY CLASSIFICATION
Hughes Tool Company - Aircraft Division	Unclassified
Culver City, California	2b. GROUP
	- - -

3. REPORT TITLE

ROTOR/WING
FINAL TECHNICAL REPORT

4. DESCRIPTIVE NOTES *(Type of report and inclusive dates)*
Summary Report of Rotor/Wing Research

5. AUTHOR(S) *(First name, middle initial, last name)*

F. J. Briardy
S. V. LaForge
J. R. Neff

6. REPORT DATE	7a. TOTAL NO. OF PAGES	7b. NO. OF REFS
March 1970	79	23

8a. CONTRACT OR GRANT NO.	9a. ORIGINATOR'S REPORT NUMBER(S)
Nonr-4588(00) NR 212-162	
b. PROJECT NO.	HTC-AD 69-12A
N/A	(397-X-8002)
c.	9b. OTHER REPORT NO(S) *(Any other numbers that may be assigned this report)*
d.	

10. DISTRIBUTION STATEMENT

This document has been approved for public release and sale:
its distribution is unlimited.

11. SUPPLEMENTARY NOTES	12. SPONSORING MILITARY ACTIVITY
- - -	Office of Naval Research
	Aeronautics Code 461
	Arlington, Virginia 22217

13. ABSTRACT

This summary report presents the technical status of the Rotor/Wing concept of
a stopped-rotor helicopter configuration. The configuration presents attractive
performance characteristics for a high-speed VTOL aircraft. The ability to pre-
dict aerodynamic performance characteristics in all flight modes is substantiated
by wind-tunnel tests. A major technical problem of 3-per-rev oscillating loads
on the Rotor/Wing pylon has been minimized by the effective use of cyclic blade
pitch during the high-advance-ratio portion of conversion. High values of oscil-
lating blade-root moments have been recorded during testing of a dynamic model.
It is not known if there is a schedule of cyclic pitch that will minimize both pylon
loads and blade-root loads simultaneously.

DD FORM 1473 REPLACES DD FORM 1473, 1 JAN 64, WHICH IS
1 NOV 66 OBSOLETE FOR ARMY USE.

14 KEY WORDS	LINK A		LINK B		LINK C	
	ROLE	WT	ROLE	WT	ROLE	WT
Rotor						
Wing						
Stopped-rotor						
Conversion						
Helicopter						
Autogyro						
Airplane						
Wind tunnel test						